Article

Deformation and Transformation Textures in the NaMgF₃ Neighborite—Post-Perovskite System

Estelle E. Ledoux [1,*], Michael Jugle [1], Stephen Stackhouse [2] and Lowell Miyagi [1]

1. Department of Geology and Geophysics, University of Utah, Salt Lake City, UT 84112, USA; lowell.miyagi@utah.edu (L.M.)
2. School of Earth and Environment, University of Leeds, Leeds LS2 9JT, UK; s.stackhouse@leeds.ac.uk
* Correspondence: estelle.ledoux@utah.edu

Abstract: The D″ region of the lower mantle, which lies just above the core–mantle boundary, is distinct from the bulk of the lower mantle in that it exhibits complex seismic heterogeneity and seismic anisotropy. Seismic anisotropy in this region is likely to be largely due to the deformation-induced texture (crystallographic preferred orientation) development of the constituent mineral phases. Thus, seismic anisotropy can provide a marker for deformation processes occurring in this dynamic region of the Earth. Post-perovskite-structured (Mg,Fe)SiO₃ is believed to be the dominant mineral phase in many regions of the D″. As such, understanding deformation mechanisms and texture development in post-perovskite is important for the interpretation of observed seismic anisotropy. Here, we report on high-pressure diamond anvil cell deformation experiments on NaMgF₃ neighborite (perovskite structure) and post-perovskite. During deformation, neighborite develops a 100 texture, as has been previously observed, both in NaMgF₃ and MgSiO₃ perovskite. Upon transformation to the post-perovskite phase, an initial texture of {130} at high angles to compression is observed, indicating that the {100} planes of perovskite become the ~{130} planes of post-perovskite. Further compression results in the development of a shoulder towards (001) in the inverse pole figure. Plasticity modeling using the elasto-viscoplastic self-consistent code shows this texture evolution to be most consistent with deformation on (001)[100] with some contribution of glide on (100)[010] and (001)<110> in NaMgF₃ post-perovskite. The transformation and deformation mechanisms observed in this study in the NaMgF₃ system are consistent with the behavior generally observed in other perovskite–post-perovskite systems, including the MgSiO₃ system. This shows that NaMgF₃ is a good analog for the mantle bridgmanite and MgSiO₃ post-perovskite.

Keywords: NaMgF₃; post-perovskite; phase transformation; deformation; lattice-preferred orientation; EVPSC; D″ layer; lower mantle; anisotropy

1. Introduction

One of the most complex and enigmatic regions of the Earth's mantle is the D″ region, which occurs between the core–mantle boundary (CMB) and the D″ seismic discontinuity. Indeed, although the bulk of the lower mantle appears isotropic and seismically homogeneous (e.g., [1–4]), the D″ region is more complex and exhibits lateral heterogeneity, anisotropy, and large topographic variations of the D″ discontinuity [2,3,5–7]. In particular, global tomography models of the D″ region have revealed large-scale seismic anomalies characterized by high S-wave velocity regions beneath the circum-Pacific, and two large low shear velocity provinces (LLSVPs) beneath the central Pacific and southern Africa (e.g., [1,2,8,9]). The high-velocity regions are generally interpreted to be colder than the surrounding areas and may be remnants of slabs subducted to the CMB [10]. On the contrary, LLSVPs may be related to warm regions of upwelling (e.g., [11]) or chemical variation (e.g., [12]). Anisotropy in the D″ is complicated but generally exhibits $V_{SH} > V_{SV}$ anisotropy in the high-velocity circum-Pacific regions [1,2,8,9,13]. In the LLSVPs beneath

the central Pacific and southern Africa, anisotropy is more varied with observations of both $V_{SH} > V_{SV}$ and $V_{SV} > V_{SH}$ as well as regions of isotropy [1,2,5,6,8,9,13].

As the D″ is the lower boundary layer of the mantle, it plays an important role in mantle dynamics [14–16]. Indeed, numerical modeling and laboratory experiments seem to indicate that deformation is enhanced near boundary layers and large strain deformation is expected to occur in the D″ region [14,17,18]. Also, based on experimental and theoretical evidence, the D″ layer may be mechanically weak, leading to shear localization [19–21]. As large strains are expected to occur in the D″ layer, anisotropy in this region is generally attributed to the texture (crystallographic preferred orientation (CPO)) of the constituent mineral phases as a result of ductile deformation during mantle convection [13,14,17,21–24].

Hence, in order to interpret anisotropy in the lower-most mantle, it is critical to understand the processes that lead to texture development in the phases of interest under the appropriate conditions. MgSiO$_3$ bridgmanite (Bdm), the dominant phase in much of the lower mantle, undergoes a solid-solid phase transition from a perovskite (Prv) structure to a post-perovskite (pPrv) structure at conditions similar to the top of D″ [25–27]. For Prv to pPrv phase transitions, computational [28,29] and experimental [30–33] studies have reported possible coherent transformation mechanisms, i.e., transformation mechanisms where the daughter phase nucleates with a specific crystallographic relationship to the parent phase. The phase transition at the D″ discontinuity may hence introduce a transformation texture in the newly nucleated pPrv. This process needs to be understood in order to correctly interpret seismic anisotropy in the D″ region.

While the global presence of post-perovskite (and so the continuity of the D″ layer) is still debated, as higher temperature regions of the lowermost mantle are likely to stabilize Bdm over pPrv (e.g., [8,34,35]), and some chemical heterogeneities may lead to significant regions of Bdm and pPrv coexistence (e.g., [36]), it is now widely accepted that magnesium silicate post-perovskite (Mg-pPrv) is a major mineral phase in much of the D″ [37]. In general, texture in the lower mantle is largely due to dislocation motion and associated crystal rotations. Thus, in recent years, significant efforts both computational (e.g., [38–40]) and experimental (e.g., [41–43]) have been made to constrain slip systems in lower mantle minerals with the goal of interpreting seismic anisotropy in terms of mantle flow (e.g., [24,44]).

The high pressures and temperatures required to synthetize bridgmanite and MgSiO$_3$ pPrv make experimental measurements difficult and, although many studies have focused on slip systems and texture development in Prv and pPrv analogs, the dominant slip systems are still debated. In general, the slip plane tends to be better constrained than the slip direction; nonetheless, three sets of dominant slip systems have been proposed for pPrv: (1) slip on (010) planes, (2) slip on (100) planes and/or the {110}<1–10> slip systems, and (3) slip on the (001) planes.

Early studies proposed that slip should occur on the (010) plane based on the fact that this coincides with the layering of the SiO$_6$ octahedra in the pPrv structure [25,26,45]. Several theoretical calculations have also supported slip on (010) in pPrv analog materials. Simulations based on the Peierls–Nabarro model found (010)[001] to be the dominant slip system in MgSiO$_3$ pPrv [46,47]. Work by Metsue et al. [48] suggested that for CaIrO$_3$ pPrv, (010)[001] slip should be the easiest slip system. More recent atomic scale modeling also finds that (010)[100] slip is favored in MgSiO$_3$ pPrv [38,49,50]. Experimental evidence for slip on the (010) plane in pPrv, however, is limited to the CaIrO$_3$ analog. Due to its stability in the pPrv structure at ambient or near ambient conditions [51], CaIrO$_3$ has been the most studied for the deformation mechanisms of the pPrv-structured compounds [52–59]. Indeed, because CaIrO$_3$ pPrv is quenchable to ambient conditions, electron microscopy studies can be performed to study dislocation microstructures. In particular, transmission electron microscopy (TEM) studies have observed Burgers vectors of **b** = [100] and **b** = <u0w> [52] or **b** = [100] and **b** = [001] [60,61], suggesting that (010) is the most likely slip plane in CaIrO$_3$ pPrv. Other studies on the deformation of CaIrO$_3$, investigating different pressure and temperature conditions, all report dominant dislocation slip on the (010) planes [53–56,58,59,61]. Based on electron back-scatter diffraction (EBSD)

and/or TEM, some studies have extracted the full dominant slip system, which appears to be (010)[100] [53,54,58,59]. Using the viscoplastic self-consistent (VPSC) model [62], Miyagi et al. [56] showed that the experimental deformation texture in CaIrO$_3$ could be explained by slip on (010)[100] with some slip on (010)<101>, in agreement with electron microscopy observations. Slip on (010)[001] was rejected as it generates textures incompatible with the experiments [56]. In addition, some TEM observations report the presence of {110} twin domains [60,61], suggesting twinning may also be a possible deformation mechanism in CaIrO$_3$.

Walte et al. [58] also report transformation experiments on CaIrO$_3$ Prv to pPrv, observing that after transformation from Prv, the pPrv phase exhibited a texture of (100) planes almost normal to the compression directions. That texture, however, is rather related to the oriented growth of the pPrv, as the relict coexisting Prv grains do not show any texture.

Evidence for (100) and/or {110}<1–10> slip comes from theoretical calculations and two early diamond anvil cell (DAC) studies. First-principles metadynamics and energetics of stacking faults predicted slip on {110}<1–10> during the phase transformation from Bdm to pPrv [29]. Shortly thereafter, room temperature radial diffraction DAC experiments on MgGeO$_3$ pPrv and MgSiO$_3$ pPrv found textures characterized by (100) planes at high angles to compression [63,64]. Polycrystal plasticity modeling showed that these textures could be explained by slip on {110}<1–10> and on the (100) planes [63,64]. It is important to note that Merkel et al. [63,64] converted to the pPrv phase directly from the enstatite phase and no change in texture was observed upon further pressure increase, leading several authors to suggest that these results could be recording transformation textures rather than deformation textures [54,58,65].

Subsequent studies on MgGeO$_3$ pPrv in the DAC using axial diffraction geometry [30] and radial diffraction geometry [31] found that after conversion from the enstatite phase to the pPrv phase, (100) planes were aligned at high angles to compression consistent with the results of Merkel et al. [63,64]. Upon further compression, however, Okada et al. [30] observed changes in the axial diffraction patterns that seem to suggest that (001) planes become aligned normal to compression. This was later confirmed by experiments of Miyagi et al. [31] which also showed the initial transformation texture of (100) planes at high angles to compression, shifting to (001) upon deformation. Polycrystal plasticity modeling, which included the effect of the transformation texture, showed the evolution of a (100) texture to a (001) texture to be most consistent with dominant slip on (001)[100]. Theoretical calculations by Metsue et al. [48] also support that the easiest slip system for MgGeO$_3$ pPrv should be (001)[100].

Slip on (001) planes in the pPrv structure is supported by several diamond anvil cell experiments both at ambient conditions [30,31,42,66] and high temperature [67,68]. Miyagi et al. [42] found, in pPrv synthesized from MgSiO$_3$ glass, that an initial (001) texture was observed after conversion at 148 GPa. Upon compression to 185 GPa, this texture doubled in strength consistent with slip on the (001) plane. High-temperature deformation experiments of MnGeO$_3$ pPrv documented the development of a (001) texture during compression from 63 GPa to 105 GPa at 2000 K [67]. Deformation textures consistent with (001) slip have also been documented in MgGeO$_3$ pPrv [30,31]. More recently, Wu et al. [68] observed a (001) texture in MgSiO$_3$ during laser heating to 2500 K at 150 GPa.

It is now becoming clear that in all experiments on MnGeO$_3$ pPrv, MgGeO$_3$ pPrv, and MgSiO$_3$ pPrv, slip is on (001) and that there is no clear evidence to support deformation on (100) or {110}<1–10>. Textures previously attributed to slip on (100) and {110}<1–10> have been shown to be due to the transformation of enstatite to pPrv. The evidence that slip on (010)[100] is the dominant system in CaIrO$_3$ is clearly quite robust based on the large number of independent and consistent experimental results [53–58,60]. It is not entirely clear why CaIrO$_3$ behaves differently from the other pPrv-structured compounds. However, CaIrO$_3$ pPrv has very different structural parameters than MgSiO$_3$ pPrv, and so in terms of bond lengths, bond angles, and octahedral distortions, MgGeO$_3$ pPrv is much closer to those of MgSiO$_3$ than CaIrO$_3$ pPrv [69]. In addition, Raman spectroscopy

measurements have indicated that bonding in $CaIrO_3$ pPrv is different from other pPrv-structured compounds [70]. Also, first-principles computations find $CaIrO_3$ pPrv to have elastic properties and an electronic structure that are inconsistent with $MgSiO_3$ pPrv [71]. Thus, it appears that $CaIrO_3$ pPrv is a poor analog for the deformation behavior of Mg-pPrv. This is unfortunate, as $CaIrO_3$ pPrv is the only pPrv to be systematically studied at high temperature and varying strain rates, and that can be characterized ex-situ by electron microscopy. Due to the high pressure necessary to synthesize $MnGeO_3$ pPrv, $MgGeO_3$ pPrv, and $MgSiO_3$ pPrv, these compounds are still challenging to study and it is thus of great interest to search for other potential analogs that can be studied at lower pressures and temperatures.

$NaMgF_3$ is a promising candidate as an analog for the deformation behavior of $MgSiO_3$ pPrv. At ambient conditions, $NaMgF_3$ neighborite is isotypic with bridgmanite (*Pbnm* perovskite) and at higher pressures, displays the same sequence of phase transitions as $MgSiO_3$ (i.e., Prv to pPrv) but at a reduced pressure of ~30 GPa (e.g., [72]). $NaMgF_3$ pPrv is structurally more similar to $MgSiO_3$ pPrv than $CaIrO_3$ [69,73], indicating that it has the potential to be a good analog material to $MgSiO_3$ pPrv. Here, we report on the development of transformation and deformation textures in the $NaMgF_3$ neighborite to the pPrv system, and discuss them in order to (i) determine if $NaMgF_3$ is a good analog for $MgSiO_3$ in terms of deformation mechanisms, and (ii) test if the Prv to pPrv transformation in $NaMgF_3$ can induce a transformation texture and so participate in seismic anisotropy.

2. Materials and Methods

2.1. Samples and High-Pressure Experiments

Two experiments were performed, one at beamline 12.2.2 of the Advanced Light Source (ALS) at Lawrence Berkeley National Laboratory, Berkeley, CA, and a second run at beamline 16 ID-B of the HP-CAT sector of the Advanced Photon Source (APS) at Argonne National Laboratory, Argonne, IL. In both runs, sample starting material was finely ground polycrystalline $NaMgF_3$ neighborite. This is the same sample used in [72].

The starting material was mixed with a small amount of Pt powder (Alfa Aesar 99.95% purity Lot # F08P21) to serve as a laser absorber and pressure calibrant. In both experiments, samples were loaded into two-stage boron kapton gaskets [74]. Pressure was measured online using a third-order Birch–Murnaghan equation of state for Pt [75]. Data were collected in radial diffraction geometry, where the x-ray beam is orthogonal to the compression axis. Samples were compressed using a modified Mao–Bell-type cell with large openings for the beam in radial diffraction geometry. We choose to not use a pressure medium, so the diamonds can impose both pressure and axial differential stress on the sample. The radial diffraction geometry allows in situ measurement of texture and lattice strain development (e.g., [43]).

For run #1, conducted at the ALS, the X-ray was collimated to a 10 μm × 10 μm beam size with a wavelength of 0.49594 Å. Sample-to-detector distance, beam center, instrument broadening, and detector tilt were calibrated using a LaB_6 standard. The sample was compressed using 300 μm flat culet diamonds. The boron gasket insert had a 400 μm outer diameter with a pre-compressed thickness of ~50 μm with an 80 μm diameter sample chamber. The sample was remotely compressed to high pressure using a gas membrane. Diffraction images were recorded at regular pressure intervals using a MAR3450 image plate (Marresearch GmbH, Norderstedt, Germany) and 120 s exposure times. Pressure after closing the cell was ~3 GPa. The sample was then compressed to 27 GPa and heated to ~1400 K using single-sided laser heating to induce the transition to the pPrv phase. During the 30 min laser heating, the laser was continuously rastered across the sample to try to obtain homogeneous conversion. Temperature was kept low during laser heating, as higher temperatures induce excessive grain growth in this system. After laser heating, a two-phase mixture of neighborite and post-perovskite was observed. This mixture was then incrementally compressed up to ~44 GPa.

For run #2, conducted at the APS, beam size was 10 μm × 10 μm and the x-ray wavelength was 0.619921 Å. A CeO_2 standard was used to calibrate sample-to-detector distance, beam center, instrument broadening, and detector tilt. The sample was compressed using 200 μm flat culet diamonds. The boron gasket insert had a 350 μm outer diameter with a pre-compressed thickness of ~35 μm with a 50 μm diameter sample chamber. The sample was compressed manually. Images were collected at regular pressure intervals using a MarCCD detector (Marresearch GmbH, Norderstedt, Germany) with an 8 s exposure time. In this run, the sample was initially compressed directly to 32 GPa. The phase transformation to pPrv was induced using single-sided laser heating with a flat top geometry with a 34 μm flat top and 59 μm full width half maximum. After heating to ~1400 K for ~30 min, small peaks of the neighborite phase were observed. The sample was then compressed incrementally to 64 GPa. During compression, the remaining neighborite peaks became broad and diffuse.

2.2. Data Analysis

Diffraction images were initially processed using the Fit2d software (version 18, A. Hammersley, ESRF, Grenoble, France) [76]. Images were integrated over 5° arcs into 72 discrete spectra (Figure 1). Spectra that contained the beam stop and diamond spots were removed. The images were then analyzed using the MAUD software (version 2.998, L. Lutterotti, University of Trento, Italy) that implements the Rietveld method [77]. For these analyses, we generally followed the procedure for processing radial diffraction data outlined in Wenk et al. [78], with details as follows. Backgrounds were interpolated using 10 manually selected points on each image between diffraction peaks. A Q-space range of ~2.2 to 4.2 Å^{-1} was used for run #1 (ALS) and a Q-space range of 2.25 to 3.87 Å^{-1} was used for run #2 (APS). Images were refined for crystal lattice parameters, crystallite size, lattice strain, and texture. Popa line broadening with an isotropic size–strain model was used for the refinement of crystallite size [79]. The moment pole stress model was used to refine lattice strains and calculate stress [80,81]. A bulk path geometric mean, which is between the Voigt and Reuss models, was used for the micromechanical model [81]. To extract the Q-values for the lattice strain, the 'radial diffraction in the DAC' model available in MAUD, which fits a Q(hkl) factor to each diffraction peak based on peak displacement, was employed.
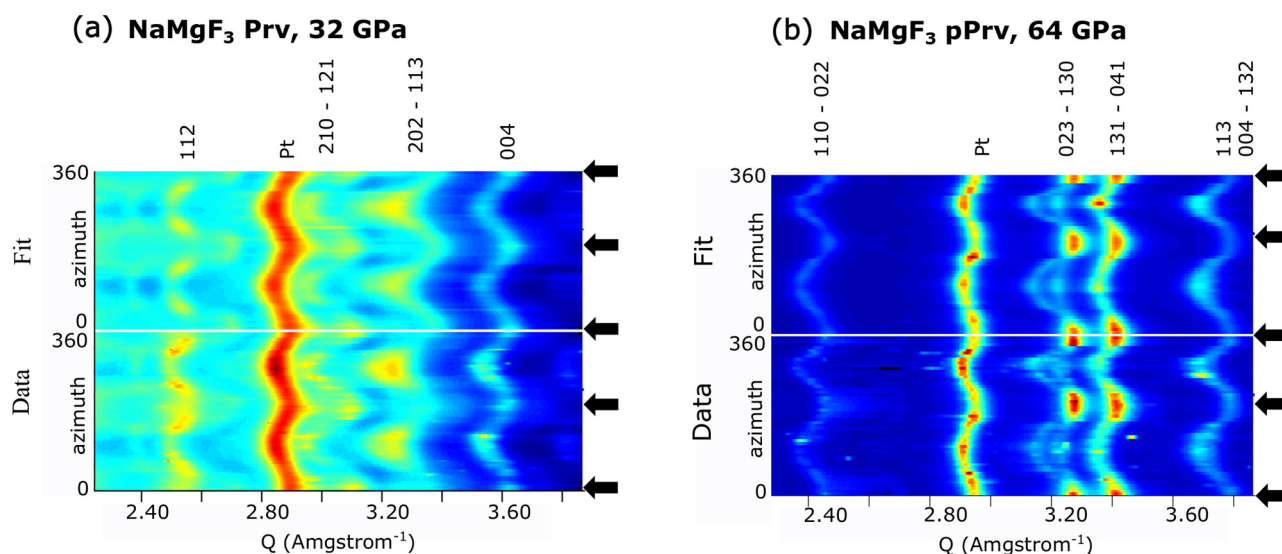

Figure 1. X-ray diffraction patterns of neighborite (**a**) and NaMgF$_3$-pPrv (**b**), from run #2. The compression direction is indicated by the bold arrows on the right side of the plots, and the main diffraction planes are labeled. Warm colors mean higher intensities.

To calculate stresses via the moment pole stress model, single crystal elastic constants (C_{ij}) and their variation with pressure are needed for neighborite and $NaMgF_3$ pPrv. Only a limited set of experimentally determined C_{ij} exists for neighborite at room pressure [82]. Thus, we chose to calculate the elastic tensor as a function of pressure for neighborite and $NaMgF_3$ pPrv (Figure 2). Density functional theory calculations [83,84] incorporating the projector-augmented wave method [85,86], were performed using VASP (5.3.5, VASP Software GmbH, Vienna, Austria) [87,88]. Elastic constants were computed for a temperature of 0 K from stress–strain relations [89], using three orthorhombic and one triclinic stress of magnitude 0.5 and 1.0%. The Perdew–Burke–Ernzerhof (PBE) exchange–correlation functional [90] was used. The kinetic-energy cut-off was 800 eV and the Brillouin zone was sampled using k-point grids [91]. This ensured that all elastic constants were converged to within two percent. For neighborite, there is excellent agreement with the ambient conditions C_{ij} of Zhao and Weidner [82], and calculated bulk modulus of Jakymiw et al. [92].
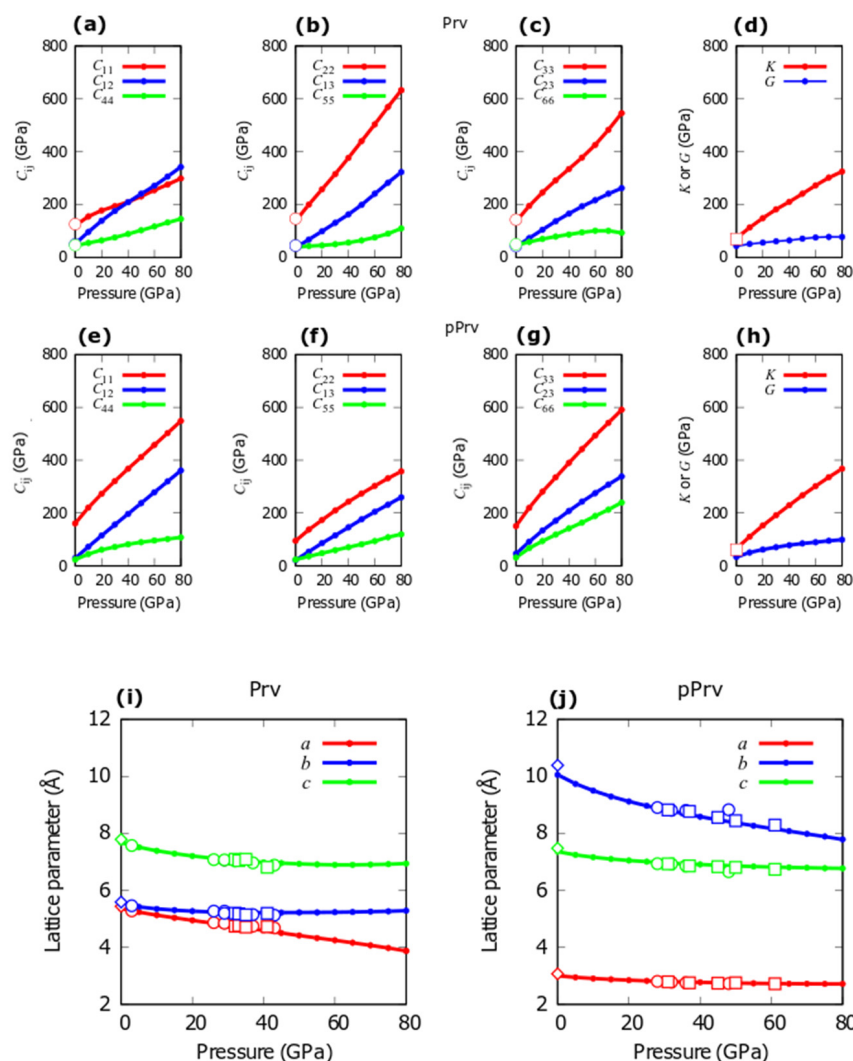

Figure 2. Elasticity models for neighborite and $NaMgF_3$ pPrv. Predicted evolution of elastic constants (C_{ij}), bulk modulus (K), and shear modulus (G) with pressure are given for neighborite (**a**–**d**) and $NaMgF_3$ pPrv (**e**–**h**). In these plots, hollow circle markers are experimental values from Zhao and Weidner [82] and square markers are data from Jakymiw et al. [92]. (**i**,**j**) show the computed evolution of the lattice parameters with pressure for neighborite and $NaMgF_3$ pPrv, respectively. Experimental lattice parameters from this study are reported in both of these plots, with circle markers corresponding to run #1 and square markers to run #2. The large diamond markers are calculated values from Arar et al. [93].

Texture analysis was performed using the E-WIMV algorithm to calculate the orientation distribution function (ODF, [94]). This is similar to the WIMV model of Matthies and Vinel [95] but allows incomplete and arbitrary pole figure coverage. A 15° ODF resolution was used. Texture was first refined without imposing symmetry to verify approximate axial symmetry about compression [95]. Cylindrical symmetry was then imposed about the compression axis, consistent with the geometry of axial compression. The ODF from MAUD was exported to Beartex [96] and smoothed with a 10° Gauss filter. Axial compression textures can be represented using an inverse pole figure (IPF). As neighborite and $NaMgF_3$ pPrv are orthorhombic, only one quadrant of the IPF is needed to represent the orientation distribution. Pole densities are displayed in multiples of random distribution (m.r.d.), where an m.r.d. of 1 represents a random distribution. For reference, the J-index [97] and M-index [98] are also given with the experimental inverse pole figures.

2.3. Texture Simulations

Numerical simulations were used to understand the mechanisms responsible for the textures observed in our experiments. The goal is to model the expected textures induced by the phase transformation and/or deformation, and compare them to our experimental results.

To test the effect of a coherent transformation from neighborite to $NaMgF_3$ pPrv, we employed the open-source MTEX toolbox for MATLAB (version 2023, MathWorks, Natick, MA, USA) [99]. For these simulations, we start from the experimental LPO of neighborite prior to the transformation, and compute the expected LPO of the daughter $NaMgF_3$ pPrv resulting from a strict coherent transformation. The computation first needs to discretize the initial Prv pre-transformation LPO by choosing randomly 500,000 orientations in the ODF. The software then applies a crystal lattice rotation to each of these grains according to the transformation relationship specified. Finally, an ODF is computed based on the new orientations obtained after the transformation operation. We test for the orientation relationships suggested in the literature, including either $[110]_{Prv}//[010]_{pPrv}$ and $[001]_{Prv}//[001]_{pPrv}$ [28], $[010]_{Prv}//[110]_{pPrv}$ and $[100]_{Prv}//[1-10]_{pPrv}$ [29], or $[010]_{Prv}//[hh0]_{pPrv}$ and $[001]_{Prv}//[001]_{pPrv}$ [32]. The simulated daughter pPrv LPO are plotted as IPF of the compression direction.

To model the effect of plastic deformation by dislocation glide on $NaMgF_3$ pPrv textures, we used an elasto-viscoplastic self-consistent (EVPSC) model [100]. This model allows simulation of both lattice strain and texture evolution during deformation by dislocation glide. In short, the model estimates the behavior of the polycrystalline aggregate from the behavior of individual crystals, and simulates the associated evolution of the microstructure (LPO, lattice strain, grain shape). Here, we use 3000 grains randomly picked from the discretized ODF of the experimental $NaMgF_3$ pPrv post-transformation texture. We assumed an equiaxed shape for these grains and applied deformation in compression by increments of $\varepsilon = 0.0025$ up to a total axial strain of 25%. The shape of the grains was free to evolve during the deformation. The stress sensitivity was fixed to $n = 3$. Based on previous studies, we considered the (010)<100>, (010)<001>, (010)<101>, (110)<−110>, (100)<010>, (001)<100>, (001)<010>, (001)<110>, (011)<100>, (100)<001>, and (110)<001> slip systems, as well as a (110)<−110> twin. Starting from the experimental post-transformation LPO, we then optimized a combination of CRSS values using trial and error in order to reproduce experimental textures and lattice parameters observed in $NaMgF_3$ pPrv during deformation.

3. Results

Table 1 summarizes the evolution of the unit cell, crystallite size, differential stress, and texture of the different phases of the sample during the experiments. Pressures calculated for the EoS for Pt [75], neighborite, and $NaMgF_3$ pPrv [70] are generally within a few GPa of each other (Table 1). Better agreement between the pressures calculated for the various phases is obtained at lower pressures and it is likely that the larger discrepancy at higher pressures is due to the effects of high differential stresses in the sample. In run #1, laser

heating resulted in incomplete conversion with ~80% volume fraction of neighborite and ~20% volume fraction of pPrv. During further compression, the volume fraction of the pPrv phase increases to ~35%. Incomplete conversion to the pPrv phase may be due to kinetics or heterogeneous laser heating of the sample. For run #2, a more complete conversion is obtained with ~30% volume fraction of neighborite and ~70% pPrv phase. Upon further compression, the neighborite peaks become very broad and weak and could not be reliably refined, and parameters are thus not reported (Table 1). Crystallite size shows a decrease in size upon compression and an increase in size during laser heating (Table 1). After conversion to the pPrv phase, crystallite sizes in the pPrv phase are significantly larger than in the coexisting neighborite phase and decrease rapidly upon compression. One should note that crystallite sizes obtained from X-ray diffraction represent coherently diffracting domains within a grain, and thus are not equivalent to grain size.

3.1. Stress Evolution

During compression before laser heating, stress levels increase in the neighborite phase, and reach a value of 4.47 GPa at 27 GPa (measured from Pt) in run #1. For run #2, we have only one measurement before the laser heating, which gives a stress of 3.40 GPa at 32 GPa. During laser heating to ~1400 K, however, stresses decrease to 0.68 GPa and 1.84 GPa for runs #1 and #2, respectively. After conversion, stresses in the pPrv phase are slightly higher than in the neighborite phase in both runs #1 and #2 (Table 1, Figure 3. Upon compression in run #1, differential stress increases at a faster rate in the pPrv phase than in the neighborite phase, but is larger in the neighborite than in the pPrv phase, except at the highest pressure of 44 GPa, where differential stresses in pPrv are 7.06 GPa versus 6.01 GPa in the neighborite phase (Table 1). In run #2, the stress levels are quite similar in between the Prv and pPrv. Differential stresses in pPrv are initially slightly higher for a given pressure in run #2 than in run #1 (2.01 at 33 GPa in run #2 vs. 1.71 at 33 GPa in run #1). However, by the highest pressures, stresses are relatively higher in run #1 than in run #2, with a differential stress of 7.06 GPa at 44 GPa for run #1 and 5.68 GPa at 64 GPa for run #2 (Table 1).

The green solid line in Figure 3 shows the evolution of the stress in the virtual sample during the EVPSC simulation of compression of the $NaMgF_3$ pPrv. Note that we make the simulation start after the phase transformation in pPrv in run #2, which means the sample is already at 33 GPa (Table 1). Based on stress measurements extracted using MAUD, at that stage of the experiment, pPrv is already under ~2 GPa of stress. The stress shown in Figure 3 (green line) is then additional stress induced by plastic deformation.

We can see that in the simulation, with increasing pressure, stress increases rapidly until reaching a plateau of ~2.1 GPa (~4.1 'total stress') at a pressure of 43 GPa. This evolution is a bit different to that which is observed in the experiment (red curve in Figure 3), where stress does not reach a plateau at 43 GPa but keeps increasing to reach a higher stress value of 5.68 GPa. That difference between the experiment and simulation may indicate that our model does not perfectly fit slip hardening.

Table 1. Unit cell parameters and calculated pressures, crystallite size, differential stress (t), and inverse pole figure first and secondary maximum for NaMgF$_3$ Prv and pPrv, for runs #1 and #2. In the following discussion, we will use the convention where negative stress values correspond to stresses in the extensional direction, and positive values to stresses in the compressional direction. Numbers in parentheses are uncertainties on the last digit estimated by the MAUD refinement. Note that these uncertainties are standard deviation from the Rietveld fit. Cell parameters and crystallite size decrease with pressure. Likewise, strain increases with pressure. The maximum m.r.d (multiples of random distribution) value of the inverse pole figure tends to decrease with increasing pressure. As can be seen in Figure 4, this maximum occurs with a (110) texture.

| Run #	Pressure (GPa)			Unit Cell Parameters							Crystallite Size		t		IPF Max (m.r.d.)		IPF Secondary Max (m.r.d.)	
				Pt	Prv				pPrv		Prv	pPrv	Prv	pPrv				
	Pt	Prv	pPrv	a(Å)	a(Å)	b(Å)	c(Å)	a(Å)	b(Å)	c(Å)	(Å)	(Å)	(GPa)	(GPa)	Prv	pPrv	Prv	pPrv
1	3	3	-	3.9121(2)	5.2831(5)	5.4631(5)	7.5713(8)	-	-	-	257(2)	-	1.91(1)	-	4.6	-	1.0	-
1	25	26	-	3.8261(2)	4.8664(13)	5.2712(12)	7.0784(14)	-	-	-	92(1)	-	4.44(4)	-	3.4	-	0.8	-
1	27	29	-	3.8216(2)	4.8491(13)	5.2702(12)	7.0527(13)	-	-	-	79(1)	-	4.47(4)	-	3.5	-	1.0	-
1	28	29	28	3.8166(1)	4.8488(9)	5.1951(9)	7.0719(11)	2.8065(3)	8.9035(13)	6.9403(8)	152(1)	3421(124)	0.68(2)	1.05(4)	2.9	4.6	1.2	none
1	33	32	32	3.8018(1)	4.8108(10)	5.1719(9)	7.0191(12)	2.7847(4)	8.8103(20)	6.9241(11)	140(1)	842(22)	2.47(3)	1.71(5)	3.8	3.9	1.4	2.2
1	40	37	36	3.7838(1)	4.7471(15)	5.1486(15)	6.9673(18)	2.7565(4)	8.8058(14)	6.8576(10)	122(1)	211(2)	3.99(2)	3.57(1)	3.6	2.6	2.2	1.7
1	44	43	48	3.7613(1)	4.6835(17)	5.1292(17)	6.8847(18)	2.7328(4)	8.8322(21)	6.6526(9)	88(1)	168(1)	6.01(4)	7.06(3)	2.3	2.9	1.7	1.3
2	32	32	-	3.8062(2)	4.7441(12)	5.1970(11)	7.0929(9)	-	-	-	135(2)	-	3.40(3)	-	2.3	-	1.6	-
2	33	33	31	3.8015(2)	4.7642(24)	5.1773(27)	7.0467(27)	2.7926(3)	8.8210(17)	6.9285(5)	288(10)	601(7)	1.84(6)	2.01(1)	1.6	2.5	-	none
2	40	35	37	3.7816(2)	4.7153(4)	5.1431(28)	7.0925(26)	2.7550(7)	8.7720(26)	6.8583(9)	190(4)	151(2)	3.26(8)	3.92(5)	-	2.9	-	none
2	49	41	45	3.7580(2)	4.7253(224)	5.1942(192)	6.8094(141)	2.7445(8)	8.5603(32)	6.8337(13)	106(9)	115(3)	4.75(44)	4.56(8)	-	3.0	-	none
2	54	-	50	3.7475(1)	-	-	-	2.7408(7)	8.4452(23)	6.8079(8)	-	89(1)	-	5.44(6)	-	3.0	-	1.3
2	64	-	61	3.7232(1)	-	-	-	2.7247(6)	8.2917(19)	6.7400(7)	-	78(1)	-	5.68(2)	-	2.6	-	1.4
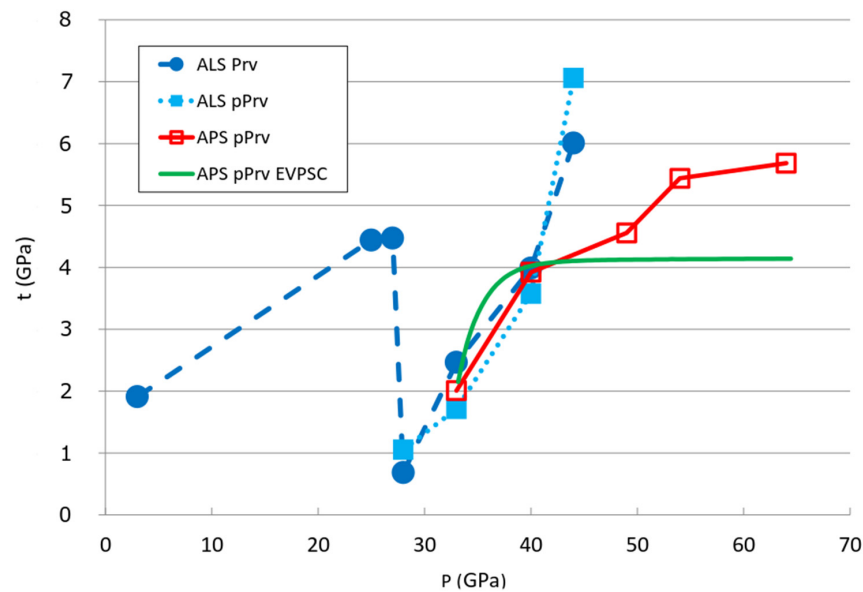
Figure 3. Stress (t) evolution with pressure (P) in the sample (Prv and pPrv) for experiments and for an EVPSC simulation. The dark blue markers are for stress in the Prv in run #1, the light blue markers are for stress in the pPrv in run #1, and the red markers are for stress in the pPrv in run #2. Stress evolution observed during the EVPSC simulation (see Section 4.4 for more details on the simulation) is reported as the green solid line.

3.2. Texture Development

In run #1, NaMgF$_3$ perovskite initially develops a strong 100 texture during compression in the DAC (Figure 4). By 3 GPa, the IPF maximum is 4.6 m.r.d. but this weakens to ~3.5 m.r.d. upon compression to 27 GPa. Similarly, in run #2, just prior to conversion, the texture in the perovskite phase exhibits a 100 maximum, but is weaker, with a 2.3 m.r.d. At pressures in excess of ~30 GPa, the neighborite develops a secondary maximum at 001 that becomes stronger upon compression (Figure 4c–e). Just after conversion, the pPrv has a maximum half way between 010 and 100 in the inverse pole figure in both runs (Figure 4f,j). Due to the large b-axis length of pPrv, this position is close to the {130} pole. Upon further compression, the 130 maximum becomes weaker and a secondary maximum near 001 develops (Figure 4g,h,k–m), but overall, the texture is still dominated by the 130 maxima. Texture strength in pPrv just after the transformation is initially stronger in run #1 (4.6 m.r.d.) than in run #2 (2.5 m.r.d.). Upon compression, however, the inverse pole figure maximum in pPrv is similar for both runs (Table 1), although closer inspection of the inverse pole figures shows that the 001 maximum is better developed in run #1 than in run #2.

3.3. Lattice Strain Evolution

The co-existence of NaMgF$_3$ Prv and pPrv in run #1 leads to significant peak overlap between the two phases. In the case of the lattice strain, it is difficult to evaluate the contribution of each phase to the overlapping peaks, and hence we decided not to use that experiment for lattice strain measurements.

The lattice strain for different crystallographic planes was fit for the NaMgF$_3$ pPrv in run #2 (Figure 5). Five crystallographic planes are considered: (022), (023), (132), (041), and (004). At 33 GPa, just after the synthesis of the NaMgF$_3$ pPrv, the lattice strain is already present, with Q-values of 0.004–0.008. With further compression, lattice strain on (023), (022), and (132) planes keep an increasing trend. For plane (041), lattice strain seems to increase until a pressure of 49 GPa, and then decrease down to 0.008 at 64 GPa. Given the large fluctuations in the fitted Q(004) values, we consider this peak unreliable when trying to match Q(hkl) values in our EVPSC simulations.

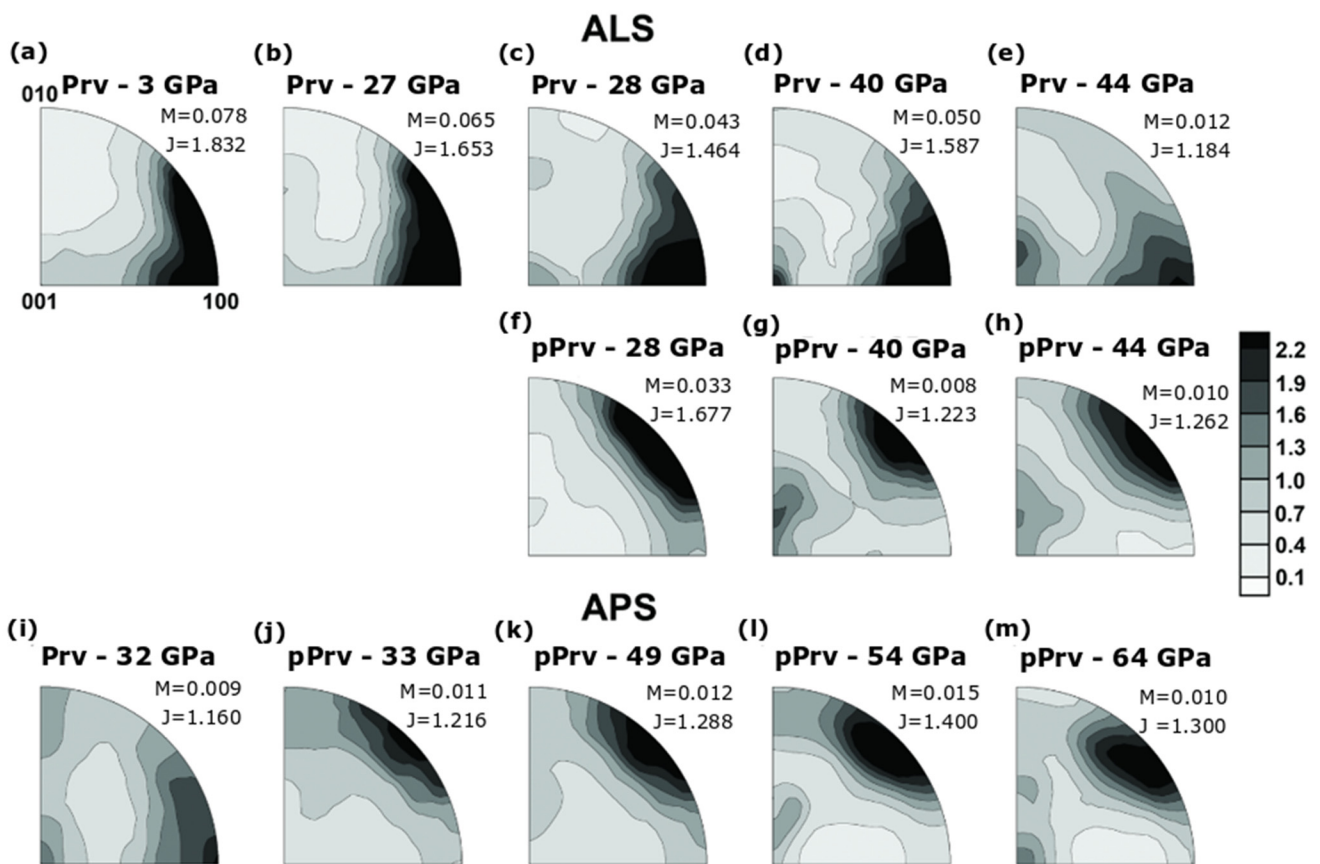**ALS**

Figure 4. Texture development in neighborite (**a**–**e**,**i**) and NaMgF$_3$ pPrv (**f**–**h**,**j**–**m**). Two runs are presented, one performed at ALS (run #1, **a**–**h**) and a second one performed at APS (run #2, **i**–**m**). The plots are IPFs of the compression direction. The scale bar on the right side is in multiple of a random distribution (m.r.d.) and applies to all the IPFs. The poles of the specific crystallographic sector used for the IPF are shown in plot (**a**). The nature of the phase considered and the measured pressure are reported on top of each IPF, and the M- and J-index of the texture strength are indicated on the side of each IPF.
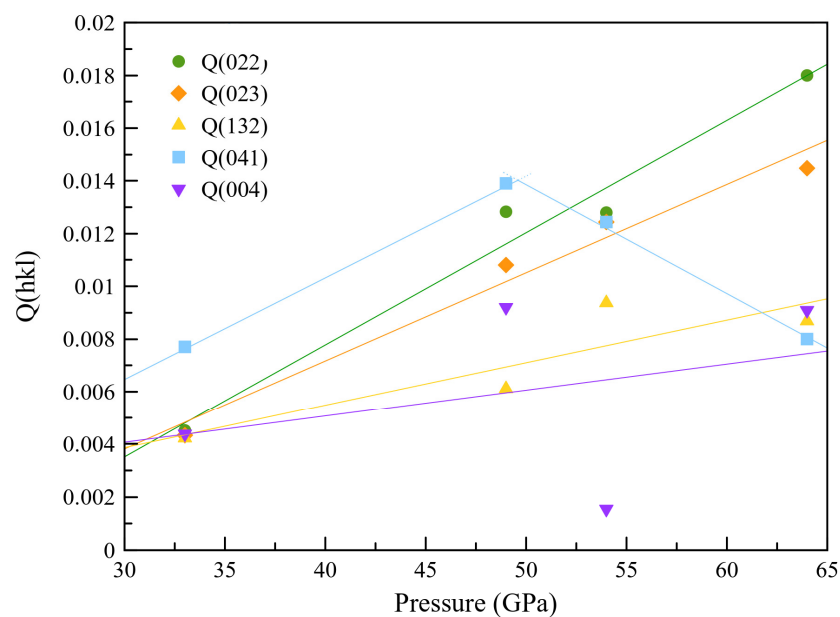
Figure 5. Lattice strain evolution in the NaMgF$_3$ pPrv of run #2 (APS).

4. Discussion

4.1. Deviatoric Stress

Previous experimental work has indicated that Prv may be mechanically stronger than the pPrv phase [19,101]. In run #1, stresses in Prv are smaller than in pPrv just after conversion. One might expect that a newly transformed phase would show lower stress levels than the parent phase, but it is possible that pPrv preferentially transforms from grains experiencing higher deviatoric stresses and thus exhibits relatively larger residual stress levels. During compression, stresses in pPrv increase more rapidly than in Prv, and at a pressure of 40 GPa, stresses are comparable in the Prv phase and the pPrv phase, with differential stress values of 3.99 GPa and 3.57 GPa, respectively (Table 1). Based on these diffraction data alone, it is difficult to tell if Prv is stronger than pPrv. The difference in the strength of the two phases in the present study is quite small (if any), while a factor of 4–5 was observed for $CaIrO_3$ and for $NaCoF_3$ [19,101]. This discrepancy may be due to microstructure, rate sensitivity, differences in strain rate between the two phases, and the fact that the DAC cannot deform at constant pressure. The presence of two phases in our samples and the microstructures of these phases can also have a significant impact on the stress distribution in between Prv and pPrv. Unfortunately, $NaMgF_3$ pPrv is not quenchable, and thus we cannot access information on microstructures such as the spatial distribution (interconnected pPrv vs. isolated crystals) of the two phases. Additionally, the work of Hunt et al. [19] and Dobson et al. [101] were performed at high temperatures, whereas our experiments are at ambient temperature. Indeed, theoretical calculations indicate that diffusion in pPrv is faster than in the Prv phase [20], and this could play a role in this discrepancy. At the highest pressure of 44 GPa in run #1, stress levels in Prv are smaller than in pPrv (6.01 GPa versus 7.06 GPa) by almost 1 GPa (Table 1). It is possible that this change of behavior is due to microstructure changes but could also be due to the fact that Prv is far outside of its stability field, which may impact the mechanical properties.

4.2. Deformation Textures in Perovskite

The initial (100) texture seen in the $NaMgF_3$ Prv phase is similar to that observed in the D-DIA on single-phase $NaMgF_3$ perovskite deformed at 3.7 GPa and 400 °C [102]. The texture strength in the D-DIA experiment, though, is much stronger, with an IPF maximum of 11.8 m.r.d. Possible explanations for this difference are multiple: it could be a difference in total strain, in temperature, and/or in potential overprinting of the (100) texture at higher pressures. At 3 GPa, total strains in DAC are much lower than in the D-DIA. Indeed, in the D-DIA experiment of Kaercher et al. [102], the total strain was 37%. In contrast, estimates for total strain acquired over the entire compression range of a DAC experiment are generally in the range of 30%–50% (e.g., [42,43,103]). Thus, at a low compression of 3 GPa in the DAC, the total strain is expected to be low. Additionally, the work of Kaercher et al. [102] was performed at 400 °C and it is possible that this elevated temperature improves the ductility of $NaMgF_3$. Finally, at higher pressures, we observe the formation of a secondary maximum near 001, and it is possible that the formation of the 001 texture results in the weakening of the initial 100 texture. The 100 texture in $NaMgF_3$ Prv was attributed to (100) slip by Kaercher et al. [102]. Miyagi and Wenk [43] also noted that twinning on {110} can produce strong 100 textures. In the work of Kaercher et al. [102], elevated temperature may suppress twinning and thus it is likely that (100) slip is dominant. In our room-temperature experiments, we cannot rule out initial {110} twinning as a possibility for the origin of the 100 texture maximum. The 001 texture observed at high pressures is unlikely to be due to twinning, as twinning is active early in deformation. Thus, we conclude that the formation of a 001 texture is most likely to be due to slip. The modeling of perovskite deformation textures by Miyagi and Wenk [43] shows that 001 textures are likely due to slip on (001) planes, but it is difficult to constrain the slip direction. Interestingly, both 001 and 100 textures have been observed during the deformation of bridgmanite. In room-temperature DAC experiments, 001 textures are most commonly observed [43,104], but at higher pressures (>55 GPa), 100 textures have also been observed in the DAC [43]. At

high temperatures, 100 textures have been observed in the large-volume press [105] and in the resistive-heated DAC [106]. In any case, it appears that both bridgmanite and $NaMgF_3$ Prv exhibit activity of slip on (100) planes [43,105,106] and (001) planes [43,57,104,107].

Furthermore, the activity of these slip systems seems to be sensitive to changing deformation conditions, illustrating the complex deformation behavior of orthorhombic perovskites.

4.3. Transformation Textures

Textures observed just prior to the phase transformation show (100) perovskite planes at high angles to compression (Figure 4b,i). Just after transformation to pPrv, {130} planes are at high angles to compression and show a similar texture strength to the 100 Prv texture (Figure 4f,j). This is consistent with a transformation mechanism where $(100)_{Prv}$ becomes $\sim\{130\}_{pPrv}$. This orientation relationship closely preserves planes of MgF_6 octahedra along $(110)_{Prv}$ with the $(010)_{pPrv}$ octahedral layers in the pPrv structure.

Up to now, orientation relationships through the Prv to pPrv transformation in the $MgSiO_3$ system could not be investigated due to the difficulties of reproducing the transformation in the laboratory. For that reason, analogs are used to study the Prv–pPrv transformation, as well as deformation in the pPrv phase.

Previous work on $NaNiF_3$ Prv and pPrv by Dobson et al. [32] documents orientation relationships in partially transformed samples. The $NaNiF_3$ pPrv phase is quenchable and orientation relationships between the Prv and pPrv phases can be analyzed directly with TEM. In their partially converted $NaNiF_3$ sample, [001] was preserved between the two structures, and orientation relationships of $(010)_{Prv}$ ~parallel to $(110)_{pPrv}$ were observed [32]. Transformation of Prv into pPrv following that transformation mechanism has also been observed in the $NaCoF_3$ system [33]. To test if that transformation mechanism could explain our experimental observations, we used the package MTEX to simulate a coherent transformation of our experimental Prv (see Section 2.3 for details) following the crystallographic relationship given by Dobson et al. [32]. The resulting pPrv texture (Figure 6c) does not resemble our $NaMgF_3$ pPrv textures: it has a strong maximum at the 010 pole and a secondary maximum in 001. Thus, that transformation mechanism is not active in our samples.

In the $MgGeO_3$ analog system, when a Prv phase with a preexisting 001 texture is converted to the pPrv phase, the pPrv phase inherits a strong 001 texture [30,31]. This indicates that $(001)_{Prv}$ becomes $(001)_{pPrv}$ in the $MgGeO_3$ system. This orientation relationship is consistent with those documented in this work (on $NaMgF_3$), in the work of Dobson et al. [32] on $NaNiF_3$, and in the work of Gay et al. [33] on $NaCoF_3$. In the $CaIrO_3$ system, a post-transformation texture with (100) planes at high angles to the compression direction has been observed in the pPrv phase [58]. However, as the $CaIrO_3$ Prv did not exhibit a significant texture prior to transformation, a transformation relationship between $CaIrO_3$ Prv and pPrv was ruled out [58].

Two computational studies have proposed mechanisms for the Prv–pPrv phase transformation in the $MgSiO_3$ system. Tsuchiya et al. [28] propose a mechanism where the phase transformation is accomplished by a rapid decrease in the γ angle of the bridgmanite unit cell. This results in the following orientation relationships between the two structures $[1–10]_{Prv} \rightarrow [100]_{pPrv}$, $[110]_{Prv} \rightarrow [010]_{pPrv}$, and $[001]_{Prv} \rightarrow [001]_{pPrv}$ [28]. Alternately, Oganov et al. [29] predicted that the Prv to pPrv transformation occurs by sliding along the Prv (010)[100] system, which becomes {110}<1–10> in pPrv. These crystallographic relationships were also tested with simulations. Figure 6c,d shows that although the two transformation mechanisms preserve the [001] direction between the two structures, i.e., the neighborite c-axis transforms to the $NaMgF_3$ pPrv c-axis, they result in different post-transformation textures. The transformation mechanism proposed by Tsuchiya et al. [28] produces a post-transformation texture with a maximum with {130} planes at high angles to compression and a secondary maximum in 001, matching our experimental pPrv post-transformation (Figure 6d). The intensity of the simulated LPO, though, is much lower

than in the experiment. That intensity difference may come from a lack of variant selection in our simulation, and/or from the calculation in MTEX, which smooths the discrete orientations when reconstructing the ODF. Another discrepancy between the simulated and experimental textures is that the 001 secondary maximum expected by the coherent transformation simulation is absent in the experimental pPrv LPO. If NaMgF$_3$ effectively transforms following this mechanism, this feature may indicate that the transformation of Prv grains with (100) planes at a high angle of the compression direction is favored, compared to grains with (001) planes at a high angle of the compression. The mechanism proposed by Oganov et al. [29] gives a different post-transformation texture, similar to the one resulting from the mechanism of Dobson et al. [32] (Figure 6e). This mechanism too does not fit our experimental observations.
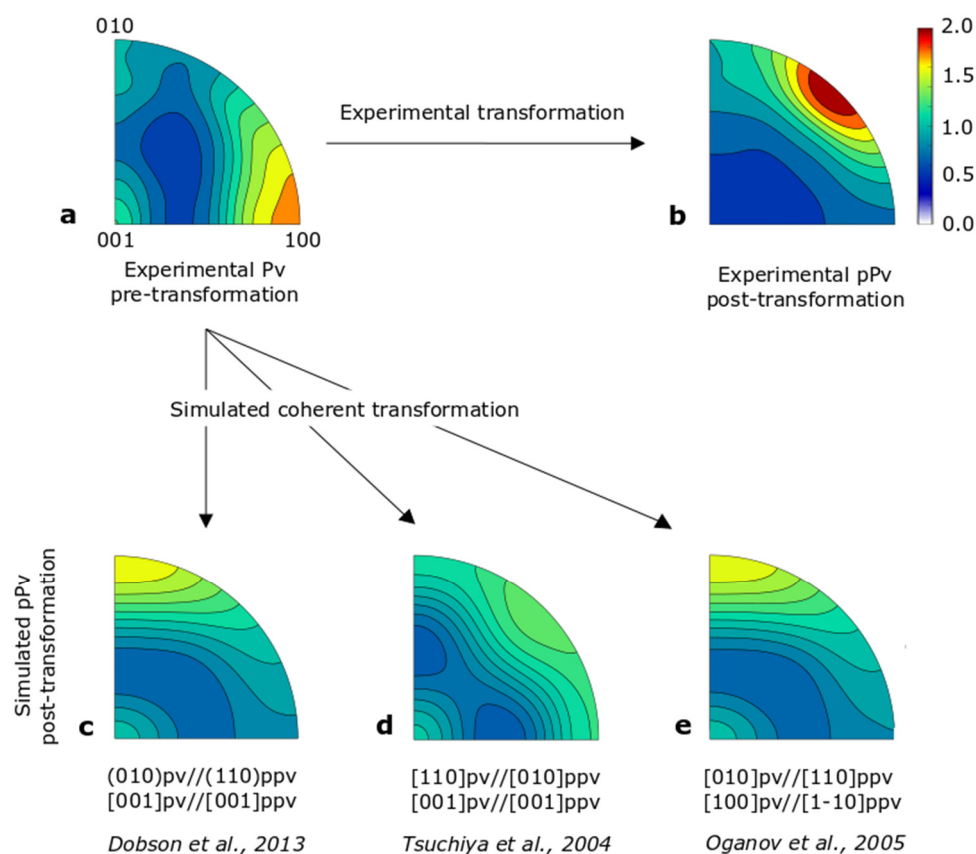
Figure 6. Simulation of coherent Prv to pPrv transformation and comparison to the experimental texture. Starting from the experimental NaMgF$_3$ Prv texture observed just before the transformation (**a**), (also shown in Figure 4i), we compute the orientations that would have the daughter pPrv grains if they transform following the crystallographic relationships proposed in Dobson et al. [32] (**c**), Tsuchiya et al. [28] (**d**), or Oganov et al. [29] (**e**). (**b**) is the experimental pPrv post-transformation texture, for comparison. Plots are IPFs of the compression direction, and the scale bar in the top right corner applies to all IPFs.

Transformation in our sample seems to follow the mechanism proposed by Tsuchiya et al. [28]. It is surprising that Tsuchiya et al. [28]'s mechanism is observed here while Dobson et al. [32]'s mechanism is reported in NaNiF$_3$ and NaCoF$_3$ [32,33]. The major difference between our work and that of Dobson et al. [32] and Gay et al. [33] is that during their experiments they heated their samples throughout the whole experiment to temperatures of ~800–1000 K, while we only used laser heating to trigger the conversion, once the Prv was already at high pressure. We are unable to determine if differences in heating path may have an impact on the transformation strongly enough to change the

transformation mechanisms, and further studies on this subject may be needed to explain these discrepancies.

Although the detailed transformation mechanisms may not be the same for $NaMgF_3$, $NaNiF_3$, $NaCoF_3$, and $MgGeO_3$ pPrv analogs, in all these compounds the Prv–pPrv transformation seems to preserve the $[001]_{Prv}//[001]_{pPrv}$ relationship. Thus, we expect that the bridgmanite in the mantle may also transform to pPrv following a coherent mechanism. However, to date, orientation relationships for silicate bridgmanite to Mg-pPrv have not yet been established experimentally.

4.4. Deformation Textures in Post-Perovskite

To interpret deformation textures in terms of the activities of deformation modes, we employ the EVPSC code. Texture evolution depends on the initial texture, the deformation geometry, the slip and twin activity, and the total strain. Since the pPrv phase has a strong initial transformation texture of {130} at high angles to compression, we adopt the approach of Miyagi et al. [31] to include the effects of transformation. We hence used the texture illustrated in Figure 4j as the starting point for the simulation. We choose to simulate the texture evolution in run #2 (APS) as we are able to obtain Q(hkl) values in this run, as there are minimal peak overlaps from the Prv phase (see Section 3.3). First, we performed a simulation using the {110} twin and the (010)[100] and (010)[001] slip systems as the easiest deformation mechanisms, as suggested by numerical computations [38,49,50]. Surprisingly, the simulation could not reproduce the experimental deformation texture and lattice strain with these parameters. Then, by using trial and error, we found a combination of CRSS for slip and twin systems modes that can fit our experimental observations. The list of slip systems considered and the associated parameters are given in Table 2.

Table 2. List of slip systems considered in our EVPSC model, the CRSS parameters used in the simulation, and the resulting activities of each slip system. The simulation applies a deformation in compression with deformation steps of 0.0025, up to a 25% total axial strain. The homogenization chosen in that simulation is the tangent model, and the stress exponent for all the slip systems is set to $n = 3$.

Slip System	CRSS	Activity (%)
(010)<100>	10	0
(010)<001>	10	0
(010)<101>	10	0
(110)<-110>	10	0
(100)<010>	0.042	35
(001)<100>	0.001	50
(001)<010>	10	0
(001)<110>	0.12	15
(011)<100>	10	0
(100)<001>	10	0
(110)<001>	10	0
(110)<−110> TWIN	10	0

Our best EVPSC fit of the experimental deformation texture is shown in Figure 7. The texture at the end of the simulation (25% axial strain, Figure 7c) reproduces the experimental texture (Figure 4m), with a strong maximum slightly shifted from 130 toward the 001 pole of the IPF, and a secondary maximum near 001. The simulated Q(hkl)s also resemble the experimental ones, showing values ranging from 0.004 to 0.016 (Figure 7b), i.e., similar to the Q-values in Figure 5, except for Q(041). This also provides a similar order of the Q(hkl)s, although the detailed evolution of Q(041) and Q(004) could not be reproduced well. The slip and twin systems activity recorded during the simulation is reported in Figure 7d, and indicates that only three slip systems are active: (001)<100>, (100)<010>, and (001)<110>. The (001)<100> is generally the most active of the slip systems, although (100)<010> contributes almost equally to the deformation at low axial strains.

The (001)<110> is weakly active at first, but its activity increases at high strain. As the activity of these three slip systems is enough to reproduce the features of our experimental observations, we can propose that these slip systems are indeed the dominant deformation mechanism in our experiments.
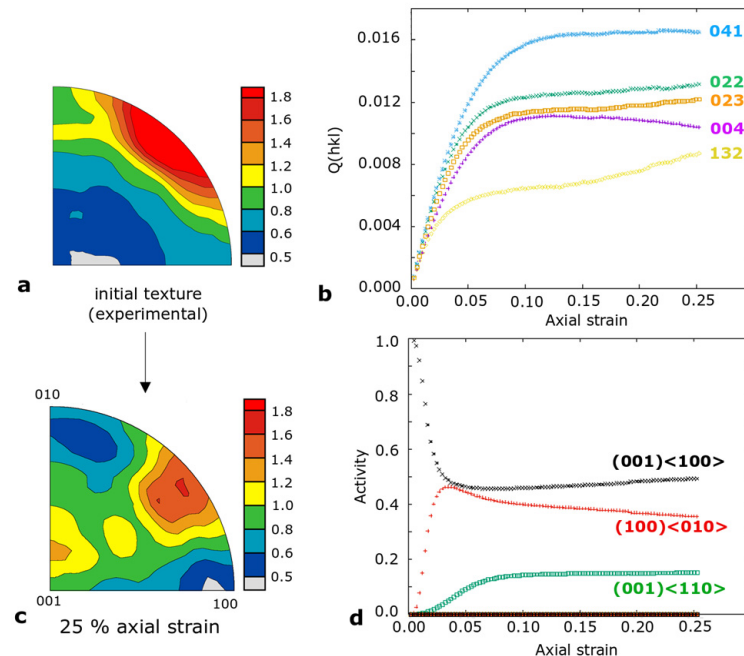

Figure 7. EVPSC fit of the experimental observations (LPO and Q-values). (**a**) Starting LPO (transformation LPO, same as Figure 4j); (**b**) Q-values evolution during the simulation; (**c**) LPO at the end of the simulation (25% axial strain); and (**d**) Slip systems (and twin) activity during the simulation. The activity curves of the three active slip systems are labeled, all the others (including the twin) have no activity.

Given the strong 130 transformation texture, it is not surprising that slip on (001) produces only weak texture development. The Schmid factor, which describes the stress resolved onto a given slip system, is defined as m = cosφcosλ, where m is the Schmid factor, φ is the angle between the slip plane normal and the applied stress, and λ is the angle between the slip direction and the applied stress. Grains with {130} at high angles to compression will have (001) planes nearly parallel to the compression direction, implying that φ will approach 90°. Thus, for these grains, the Schmid factor is close to zero and no stress is resolved onto the slip systems involving (001). Grain rotation and texture development are then restricted to those grains that are not oriented with {130} at a high angle to compression and, since the 130 transformation texture is relatively strong, most grains cannot deform efficiently by (001) slip and so texture evolution is weak. This effect will also require the activation of additional slip systems to accommodate deformation.

Dominant slip on (001) in pPrv is consistent with previous observations from the literature, where several studies report 001 textures in experimentally deformed pPrv [30,31,42,66–68]. For slip on (100) in pPrv, there is no convincing evidence in the literature. The activation of the secondary (100) slip, however, can be specific to our case, where grains are pre-oriented by the transformation in a non-favorable orientation, as discussed previously. Hence, we can propose that when pPrv transforms from a 100 textured Prv and the transformation mechanism is the same as the one observed in our experiments, (100) slip in pPrv may be needed, at least to initiate the deformation.

The consistency in observed dominant slip in NaMgF$_3$ pPrv and MgSiO$_3$ pPrv (or other structurally close pPrv) hence indicates that the NaMgF$_3$ system is a good analog for the mantle MgSiO$_3$ Prv and pPrv.

4.5. Application to the Lowermost Mantle

Textures compatible with multiple slip systems have been observed at high pressures for Bdm and its orthorhombic analogs (e.g., [108]). Two general texture types have been observed, compatible with slip on (001) planes [43,63,64] or on (100) planes [43,102,105]. Several studies have investigated the effect of slip on (001) planes with relation to anisotropy development in the lower mantle. Slip on (001) in Bdm generates shear wave splitting characterized by $V_{SV} > V_{SH}$ for waves propagating along the core–mantle boundary [23,24]. In the lowermost mantle, this is generally inconsistent with the shear wave splitting observed in the circum-Pacific region but could be compatible with regions below the central Pacific and South Africa (e.g., [1,9]). VPSC-modeled textures for slip on (100) in Bdm [106], as well as shear fabrics from experiments [105], would generate $V_{SH} > V_{SV}$ splitting for a wave propagating along the CMB, assuming a horizontal shear plane. This could be compatible with anisotropy in the circum-Pacific region, though one might expect this region to be dominated by pPrv.

Texture inheritance is likely to play an important role in anisotropy development in slabs subducted to the D″ (e.g., [32]). Currently, texture inheritance during Prv to pPrv transformation has been observed in all explored pPrv analogs except for $CaIrO_3$. As a slab is subducted, it will first deform in the Bdm stability field and, with continued subduction, transform to the pPrv phase. If Bdm in the slab is textured when it transforms to Mg-pPrv, we can then expect pPrv to inherit texture from the Bdm phase. Accordingly, complex anisotropy is observed near regions of slab subduction [109] and this may be due to the phase transformation from Bdm to Mg-pPrv [110]. Currently, most models of seismic anisotropy in the D″ ignore texture inheritance and assume a random starting texture for Mg-pPrv. In addition, texture inheritance can also be important when material upwells from the D″ and retrogrades from Mg-pPrv to Bdm. Furthermore, the most active slip system in Bdm, (001) versus (100) slip, will have a significant impact on anisotropy evolution related to the phase transformation. Two studies have been performed using transformation mechanisms proposed by Dobson et al. [32]. Walker et al. [111] assume slip on (100)[010] and then apply the orientation relationships of Dobson et al. [32]. Chandler et al. [112] assume dominant slip in Bdm on (001) planes and in multiple directions in a three-phase aggregate of Bdm, Ferropericlase, and $CaSiO_3$ Prv. Likewise, the transformation relationship of Dobson et al. [32] is used to simulate anisotropy related to the phase transformation to pPrv. Interestingly, both of these studies provide reasonable matches to anisotropy observed in global tomography models [111,112].

One complication that bears further study is the role of variant selection for anisotropy related to the Bdm to pPrv phase transformation. In high-symmetry materials, if variant selection (the preference of a transformation variant over other possible variants) is not active, textures will randomize through a martensitic phase transformation. However, frequently texture is preserved during a phase transformation, and variant selection in high-pressure experiments can be attributed to deviatoric stresses (e.g., [113]). For the Bdm to pPrv transformation, there are no symmetric variants for the $(001)_{Prv}$ to $(001)_{pPrv}$ relationship. However, there are two symmetric variants for $(100)_{Prv}$ to $\{130\}_{pPrv}$, as well as for the $(010)_{Prv}$ to $\{110\}_{pPrv}$. If deviatoric stress drives variant selection for this system, in the deep earth threshold, stresses are likely too low to drive variant selection. In this case, we would expect the $(001)_{Prv}$ to $(001)_{pPrv}$ relationship to be preserved, resulting in a strong anisotropy inheritance. However, for the $(100)_{Prv}$ to $\{130\}_{pPrv}$ and the $(010)_{Prv}$ to $\{110\}_{pPrv}$ relationships, we would expect texture strength to be approximately halved. As a result, some orientations would experience weakened texture and anisotropy. Thus, anisotropy inheritance is likely more complex than a simple transformation according to the proposed relationships, as some rotational randomization about [001] may occur. The exact nature of variant selection and threshold stresses to drive variant selection are not well understood, and it is not clear if the same transformation mechanism will apply for forward and reverse transformations.

Slip on (001) pPrv, as observed in this study, is consistent with most other pPrv-structured compounds, and generally appears to provide a good match to shear wave splitting in the circum-Pacific region [23,24,42,111,114]. Other studies, though, show a better fit using other slip systems such as (010) or (100) planes for anisotropy under the Pacific and southern Africa [115] or under subduction zones [116].

Another interesting topic that we could not investigate here is the stress dependency of the active slip systems in pPrv. Indeed, the lower stresses expected in the mantle compared to experiments may change the dominant slip system accommodating the deformation in minerals (e.g., [117]). In the current study, we do not have the method and the data to test such a possibility: stress in the DAC is high and difficult to control, and data on pressure/stress dependency of slip systems in $NaMgF_3$ pPrv are lacking. Hence, we focus here on showing that $NaMgF_3$ pPrv has similar active slip systems as $MgSiO_3$, at the lower pressure, where the pPrv phase is stable. This implies that $NaMgF_3$ is a good analog for $MgSiO_3$ pPrv, and could be used in a lower-pressure apparatus better adapted to controlled strain rate deformation than the DAC.

5. Conclusions

To study transformation and deformation mechanisms in the $NaMgF_3$ Prv–pPrv system, we performed compression experiments in the radial laser-heated DAC. $NaMgF_3$ Prv was first compressed to ~30 GPa and then converted to the pPrv phase by laser heating at ~1400 K. The obtained pPrv or Prv + pPrv polycrystals were then further compressed up to ~64 GPa. Texture, lattice strain, and differential stress in the samples were characterized in situ by X-ray diffraction. We observe a 100 texture in the deformed Prv (with an additional 001 maximum at higher pressures), a 130 transformation texture in the synthetized pPrv, and the appearance of a 001 secondary maximum in pPrv with increasing deformation. During compression, we measure high stresses in both the Prv and pPrv phases, except after laser heating, which strongly decreases stress in the remnant Prv. Overall, Prv seems stronger than pPrv. Lattice strains are also quite large in the pPrv, with Q-values of up to ~0.018.

The 100 texture observed in our deformed Prv can be related either to dislocation slip on the (100) planes or to {110} twinning. The secondary maximum in 001 appearing at higher pressures can be explained by slip on (001) planes.

Transformation simulations based on topotactic relationships show that the Prv–pPrv transformation in our samples seems to follow the crystallographic relationship given by Tsuchiya et al. [28]: $[1\bar{1}0]_{Prv}//[100]_{pPrv}$, $[110]_{Prv}//[010]_{pPrv}$, and $[001]_{Prv}//[001]_{pPrv}$. This induces a texture inheritance from the Prv to the pPrv, where the 100 texture of the parent Prv becomes a 130 texture in the daughter pPrv.

Later deformation of the pPrv leads to slight changes in the position of the 130 maximum and the appearance of a secondary 001 maximum. EVPSC models show that this texture evolution with deformation results from dislocation slip on (001)<100> and (100)<010> with some contribution of (001)<110>.

Overall, deformation in neighborite and $NaMgF_3$ pPrv is consistent with deformation mechanisms observed in other Prv and pPrv analogs (except $CaIrO_3$). Transformation mechanisms may be different from those of the $NaNiF_3$, $NaCoF_3$, or $MgGeO_3$ systems; nevertheless, they remain coherent and preserve the *c*-axis between the Prv and pPrv structures.

Author Contributions: Conceptualization, L.M.; formal analysis, M.J., L.M., S.S. and E.E.L.; investigation, L.M.; writing—original draft preparation, L.M., M.J. and E.E.L.; writing—review and editing, M.J., L.M., E.E.L. and S.S.; visualization, L.M., S.S. and E.E.L.; supervision, L.M.; project administration, L.M.; funding acquisition, L.M. All authors have read and agreed to the published version of the manuscript.

References

1. Panning, M.; Romanowicz, B. A three-dimensional radially anisotropic model of shear velocity in the whole mantle. *Geophys. J. Int.* **2006**, *167*, 361–379. [CrossRef]
2. Panning, M.P.; Lekić, V.; Romanowicz, B.A. Importance of crustal corrections in the development of a new global model of radial anisotropy. *J. Geophys. Res. Solid Earth* **2010**, *115*, B12325. [CrossRef]
3. Chang, S.J.; Ferreira, A.M.; Ritsema, J.; van Heijst, H.J.; Woodhouse, J.H. Global radially anisotropic mantle structure from multiple datasets: A review, current challenges, and outlook. *Tectonophysics* **2014**, *617*, 1–19. [CrossRef]
4. French, S.W.; Romanowicz, B.A. Whole-mantle radially anisotropic shear velocity structure from spectral-element waveform tomography. *Geophys. J. Int.* **2014**, *199*, 1303–1327. [CrossRef]
5. Cottaar, S.; Romanowicz, B. Observations of changing anisotropy across the southern margin of the African LLSVP. *Geophys. J. Int.* **2013**, *195*, 1184–1195. [CrossRef]
6. Lynner, C.; Long, M.D. Lowermost mantle anisotropy and deformation along the boundary of the African LLSVP. *Geophys. Res. Lett.* **2014**, *41*, 3447–3454. [CrossRef]
7. Ford, H.A.; Long, M.D. A regional test of global models for flow, rheology, and seismic anisotropy at the base of the mantle. *Phys. Earth Planet. Inter.* **2015**, *245*, 71–75. [CrossRef]
8. Lay, T.; Garnero, E.J. Reconciling the Post-Perovskite Phase with Seismological Observations of Lowermost Mantle Structure. In *Post-Perovskite, The Last Mantle Phase Transition*; Hirose, K., Yuen, D., Lay, T., Brodholt, J.P., Eds.; American Geophysical Union: Washington, DC, USA, 2007; pp. 129–154.
9. Kustowski, B.; Ekström, G.; Dziewoński, A.M. Anisotropic shear-wave velocity structure of the Earth's mantle: A global model. *J. Geophys. Res. Solid Earth* **2008**, *113*, B06306. [CrossRef]
10. Lithgow-Bertelloni, C.; Richards, M.A. The dynamics of Cenozoic and Mesozoic plate motions. *Rev. Geophys.* **1998**, *36*, 27–78. [CrossRef]
11. Davies, D.R.; Goes, S.; Lau, H.C.P. Thermally dominated deep mantle LLSVPs: A review. In *The Earth's Heterogeneous Mantle: A Geophysical, Geodynamical, and Geochemical Perspective*; Springer: Cham, Switzerland, 2015; pp. 441–477.
12. Zhao, C.; Garnero, E.J.; McNamara, A.K.; Schmerr, N.; Carlson, R.W. Seismic evidence for a chemically distinct thermochemical reservoir in Earth's deep mantle beneath Hawaii. *Earth Planet. Sci. Lett.* **2015**, *426*, 143–153. [CrossRef]
13. Wookey, J.; Kendall, J. Seismic anisotropy of post-perovskite and the lowermost mantle. In *Post-Perovskite, The Last Mantle Phase Transition*; Hirose, K., Yuen, D., Lay, T., Brodholt, J.P., Eds.; American Geophysical Union: Washington, DC, USA, 2007; pp. 171–189.
14. McNamara, A.K.; van Keken, P.E.; Karato, S.-I. Development of anisotropic structure in the Earth's lower mantle by solid-state convection. *Nature* **2002**, *416*, 310–314. [CrossRef]
15. Nakagawa, T.; Tackley, P.J. Effects of low-viscosity post-perovskite on thermo-chemical mantle convection in a 3-D spherical shell. *Geophys. Res. Lett.* **2011**, *38*, L04309. [CrossRef]
16. Samuel, H.; Tosi, N. The influence of post-perovskite strength on the Earth's mantle thermal and chemical evolution. *Earth Planet. Sci. Lett.* **2012**, *323*, 50–59. [CrossRef]
17. McNamara, A.K.; Keken, P.E.V.; Karato, S.-I. Development of finite strain in the convecting lower mantle and its implications for seismic anisotropy. *J. Geophys. Res.* **2003**, *108*, 2230. [CrossRef]
18. Loubet, N.; Ribe, N.M.; Gamblin, Y. Deformation modes of subducted lithosphere at the core-mantle boundary: An experimental investigation. *Geochem. Geophys. Geosyst.* **2009**, *10*, Q10004. [CrossRef]
19. Hunt, S.A.; Weidner, D.J.; Li, L.; Wang, L.; Walte, N.P.; Brodholt, J.P. Weakening of calcium iridate during its transformation from perovskite to post-perovskite. *Nat. Geosci.* **2009**, *2*, 794–797. [CrossRef]
20. Ammann, M.W.; Brodholt, J.P.; Wookey, J.; Dobson, D.P. First-principles constraints on diffusion in lower-mantle minerals and a weak D″ layer. *Nature* **2010**, *465*, 462–465. [CrossRef] [PubMed]

21. Dobson, D.P.; Lindsay-Scott, A.; Hunt, S.A.; Bailey, E.; Wood, I.G.; Brodholt, J.P.; Wheeler, J. Anisotropic diffusion creep in postperovskite provides a new model for deformation at the core-mantle boundary. *Proc. Natl. Acad. Sci. USA* **2019**, *116*, 26389–26393. [CrossRef] [PubMed]

22. Karato, S.-I. Seismic Anisotropy in the Deep Mantle, Boundary Layers and the Geometry of Mantle Convection. *Pure Appl. Geophys.* **1998**, *151*, 565–587. [CrossRef]

23. Wenk, H.R.; Cottaar, S.; Tomé, C.N.; McNamara, A.; Romanowicz, B. Deformation in the lowermost mantle: From polycrystal plasticity to seismic anisotropy. *Earth Planet. Sci. Lett.* **2011**, *306*, 33–45. [CrossRef]

24. Cottaar, S.; Li, M.; McNamara, A.K.; Romanowicz, B.; Wenk, H.R. Synthetic seismic anisotropy models within a slab impinging on the core–mantle boundary. *Geophys. J. Int.* **2014**, *199*, 164–177. [CrossRef]

25. Murakami, M.; Hirose, K.; Kawamura, K.; Sata, N.; Ohishi, Y. Post-Perovskite Phase Transition in $MgSiO_3$. *Science* **2004**, *304*, 855–858. [CrossRef]

26. Oganov, A.R.; Ono, S. Theoretical and experimental evidence for a post-perovskite phase of $MgSiO_3$ in Earth's D″ layer. *Nature* **2004**, *430*, 445–448. [CrossRef]

27. Shim, S.; Duffy, T.S.; Jeanloz, R.; Shen, G. Stability and crystal structure of $MgSiO_3$ perovskite to the core-mantle boundary. *Geophys. Res. Lett.* **2004**, *31*, L10603. [CrossRef]

28. Tsuchiya, T.; Tsuchiya, J.; Umemoto, K.; Wentzcovitch, R.M. Phase transition in $MgSiO_3$ perovskite in the earth's lower mantle. *Earth Planet. Sci. Lett.* **2004**, *224*, 241–248.

29. Oganov, A.R.; Martonak, R.; Laio, A.; Raiteri, P.; Parrinello, M. Anisotropy of Earth's D″ layer and stacking faults in the $MgSiO_3$ post-perovskite phase. *Nature* **2005**, *438*, 1142–1144. [CrossRef] [PubMed]

30. Okada, T.; Yagi, T.; Niwa, K.; Kikegawa, T. Lattice-preferred orientations in post-perovskite-type $MgGeO_3$ formed by transformations from different pre-phases. *Phys. Earth Planet. Inter.* **2010**, *180*, 195–202. [CrossRef]

31. Miyagi, L.; Kanitpanyacharoen, W.; Stackhouse, S.; Militzer, B.; Wenk, H. The enigma of post-perovskite anisotropy: Deformation versus transformation textures. *Phys Chem Miner.* **2011**, *38*, 665–678. [CrossRef]

32. Dobson, D.P.; Miyajima, N.; Nestola, F.; Alvaro, M.; Casati, N.; Liebske, C.; Wood, I.G.; Walker, A.M. Strong inheritance of texture between perovskite and post-perovskite in the D″ layer. *Nat. Geosci.* **2013**, *6*, 575–578. [CrossRef]

33. Gay, J.P.; Miyagi, L.; Couper, S.; Langrand, C.; Dobson, D.P.; Liermann, H.P.; Merkel, S. Deformation of $NaCoF_3$ perovskite and post-perovskite up to 30 GPa and 1013 K: Implications for plastic deformation and transformation mechanism. *Eur. J. Mineral.* **2021**, *33*, 591–603. [CrossRef]

34. Hernlund, J.W.; Thomas, C.; Tackley, P.J. A doubling of the post-perovskite phase boundary and structure of the Earth's lowermost mantle. *Nature* **2005**, *434*, 882–886. [CrossRef] [PubMed]

35. Van der Hilst, R.D.; De Hoop, M.V.; Wang, P.; Shim, S.H.; Ma, P.; Tenorio, L. Seismostratigraphy and thermal structure of Earth's core-mantle boundary region. *Science* **2007**, *315*, 1813–1817. [CrossRef] [PubMed]

36. Grocholski, B.; Catalli, K.; Shim, S.H.; Prakapenka, V. Mineralogical effects on the detectability of the postperovskite boundary. *Proc. Natl. Acad. Sci. USA* **2012**, *109*, 2275–2279. [CrossRef] [PubMed]

37. Cobden, L.; Mosca, I.; Trampert, J.; Ritsema, J. On the likelihood of post-perovskite near the core–mantle boundary: A statistical interpretation of seismic observations. *Phys. Earth Planet. Inter.* **2012**, *210*, 21–35. [CrossRef]

38. Goryaeva, A.M.; Carrez, P.; Cordier, P. Modeling defects and plasticity in MgSiO3 post-perovskite: Part 2—Screw and edge [100] dislocations. *Phys. Chem. Miner.* **2015**, *42*, 793–803. [CrossRef]

39. Amodeo, J.; Merkel, S.; Tromas, C.; Carrez, P.; Korte-Kerzel, S.; Cordier, P.; Chevalier, J. Dislocations and plastic deformation in MgO crystals: A review. *Crystals* **2018**, *8*, 240. [CrossRef]

40. Kraych, A.; Carrez, P.; Cordier, P. On dislocation glide in $MgSiO_3$ bridgmanite at high-pressure and high-temperature. *Earth Planet. Sci. Lett.* **2016**, *452*, 60–68. [CrossRef]

41. Girard, J.; Chen, J.; Raterron, P. Deformation of periclase single crystals at high pressure and temperature: Quantification of the effect of pressure on slip-system activities. *J. Appl. Phys.* **2012**, *111*, 112607. [CrossRef]

42. Miyagi, L.; Kanitpanyacharoen, W.; Kaercher, P.; Lee, K.K.; Wenk, H.R. Slip systems in $MgSiO_3$ post-perovskite: Implications for D″ anisotropy. *Science* **2010**, *329*, 1639–1641. [CrossRef]

43. Miyagi, L.; Wenk, H.R. Texture development and slip systems in bridgmanite and bridgmanite+ ferropericlase aggregates. *Phys. Chem. Miner.* **2016**, *43*, 597–613. [CrossRef]

44. Nowacki, A.; Nowacki, A. Predicting lowermost mantle anisotropy using models of mantle flow. In *Plate Deformation from Cradle to Grave: Seismic Anisotropy and Deformation at Mid-Ocean Ridges and in the Lowermost Mantle*; Springer: Berlin/Heidelberg, Germany, 2013; Springer Thesis; pp. 123–149.

45. Iitaka, T.; Hirose, K.; Kawamura, K.; Murakami, M. The elasticity of the $MgSiO_3$ post-perovskite phase in the Earth's lowermost mantle. *Nature* **2004**, *430*, 442–445. [CrossRef] [PubMed]

46. Carrez, P.; Ferré, D.; Cordier, P. Peierls-Nabarro model for dislocations in $MgSiO_3$ post-perovskite calculated at 120 GPa from first principles. *Philos. Mag.* **2007**, *87*, 3229–3247. [CrossRef]

47. Carrez, P.; Ferré, D.; Cordier, P. Implications for plastic flow in the deep mantle from modelling dislocations in $MgSiO_3$ minerals. *Nature* **2007**, *446*, 68–70. [CrossRef] [PubMed]

48. Metsue, A.; Carrez, P.; Mainprice, D.; Cordier, P. Numerical modelling of dislocations and deformation mechanisms in $CaIrO_3$ and $MgGeO_3$ post-perovskites—Comparison with $MgSiO_3$ post-perovskite. *Phys. Earth Planet. Inter.* **2009**, *174*, 165–173. [CrossRef]

49. Goryaeva, A.M.; Carrez, P.; Cordier, P. Low viscosity and high attenuation in MgSiO₃ post-perovskite inferred from atomic-scale calculations. *Sci. Rep.* **2016**, *6*, 34771. [CrossRef] [PubMed]

50. Goryaeva, A.M.; Carrez, P.; Cordier, P. Modeling defects and plasticity in MgSiO₃ post-perovskite: Part 3—Screw and edge [001] dislocations. *Phys. Chem. Miner.* **2017**, *44*, 521–533. [CrossRef] [PubMed]

51. Rodi, V.; Babel, D. Ternäre Oxide der Übergangsmetalle, I.V. Erdalkaliiridium(IV)-oxide: Kristallstruktur von CaIrO₃. *Z. Für Anorg. Und Allg. Chem.* **1965**, *366*, 17–23. [CrossRef]

52. Miyajima, N.; Ohgushi, K.; Ichihara, M.; Yagi, T. Crystal morphology and dislocation microstructures of CaIrO₃: A TEM study of an analogue of the MgSiO₃ post-perovskite phase. *Geophys. Res. Lett.* **2006**, *33*, L12302. [CrossRef]

53. Yamazaki, D.; Yoshino, T.; Ohfuji, H.; Ando, J.; Yoneda, A. Origin of seismic anisotropy in the D″ layer inferred from shear deformation experiments on post-perovskite phase. *Earth Planet. Sci. Lett.* **2006**, *252*, 372–378. [CrossRef]

54. Walte, N.; Heidelbach, F.; Miyajima, N.; Frost, D. Texture development and TEM analysis of deformed CaIrO₃: Implications for the D″ layer at the core-mantle boundary. *Geophys. Res. Lett.* **2007**, *34*, L08306. [CrossRef]

55. Niwa, K.; Yagi, T.; Ohgushi, K.; Merkel, S.; Miyajima, N.; Kikegawa, T. Lattice preferred orientation in CaIrO₃ perovskite and post-perovskite formed by plastic deformation under pressure. *Phys. Chem. Miner.* **2007**, *34*, 679–686. [CrossRef]

56. Miyagi, L.; Nishiyama, N.; Wang, Y.; Kubo, A.; West, D.V.; Cava, R.J.; Duffy, T.S.; Wenk, H.-R. Deformation and texture development in CaIrO₃ post-perovskite phase up to 6 GPa and 1300 K. *Earth Planet. Sci. Lett.* **2008**, *268*, 515–525. [CrossRef]

57. Miyajima, N.; Walte, N. Burgers vector determination in deformed perovskite and post-perovskite of CaIrO₃ using thickness fringes in weak-beam dark-field images. *Ultramicroscopy* **2009**, *109*, 683–692. [CrossRef] [PubMed]

58. Walte, N.P.; Heidelbach, F.; Miyajima, N.; Frost, D.J.; Rubie, D.C.; Dobson, D.P. Transformation textures in post-perovskite: Understanding mantle flow in the D″ layer of the Earth. *Geophys. Res. Lett.* **2009**, *36*, L04302. [CrossRef]

59. Hunt, S.A.; Walker, A.M.; Mariani, E. In-situ measurement of texture development rate in CaIrO₃ post-perovskite. *Phys. Earth Planet. Inter.* **2016**, *257*, 91–104. [CrossRef]

60. Miyajima, N.; Niwa, K.; Heidelbach, F.; Yagi, T.; Ohgushi, K. Deformation microtextures in CaIrO₃ post-perovskite under high stress conditions using a laser-heated diamond anvil cell. *J. Phys. Conf. Ser.* **2010**, *215*, 012097. [CrossRef]

61. Niwa, K.; Miyajima, N.; Seto, Y.; Ohgushi, K.; Gotou, H.; Yagi, T. In situ observation of shear stress-induced perovskite to post-perovskite phase transition in CaIrO₃ and the development of its deformation texture in a diamond-anvil cell up to 30 GPa. *Phys. Earth Planet. Inter.* **2012**, *194*, 10–17. [CrossRef]

62. Lebensohn, R.; Tomé, C. A self-consistent viscoplastic model: Prediction of rolling textures of anisotropic polycrystals. *Mater. Sci. Eng. A* **1994**, *175*, 71–82. [CrossRef]

63. Merkel, S.; Kubo, A.; Miyagi, L.; Speziale, S.; Duffy, T.S.; Mao, H.K.; Wenk, H.R. Plastic Deformation of MgGeO₃ Post-Perovskite at Lower Mantle Pressures. *Science* **2006**, *311*, 644–646. [CrossRef]

64. Merkel, S.; McNamara, A.K.; Kubo, A.; Speziale, S.; Miyagi, L.; Meng, Y.; Duffy, T.S.; Wenk, H.R. Deformation of (Mg,Fe)SiO₃ Post-Perovskite and D″ Anisotropy. *Science* **2007**, *316*, 1729–1732. [CrossRef]

65. Santillán, J.; Shim, S.H.; Shen, G.; Prakapenka, V.B. High-pressure phase transition in Mn2O3: Application for the crystal structure and preferred orientation of the CaIrO₃ type. *Geophys. Res. Lett.* **2006**, *33*, L15307. [CrossRef]

66. Nisr, C.; Ribárik, G.; Ungár, T.; Vaughan, G.B.; Cordier, P.; Merkel, S. High resolution three-dimensional X-ray diffraction study of dislocations in grains of MgGeO₃ post-perovskite at 90 GPa. *J. Geophys. Res. Solid Earth* **2012**, *117*, B033201. [CrossRef]

67. Hirose, K.; Nagaya, Y.; Merkel, S.; Ohishi, Y. Deformation of MnGeO3 post-perovskite at lower mantle pressure and temperature. *Geophys. Res. Lett.* **2010**, *37*, L20302. [CrossRef]

68. Wu, X.; Lin, J.F.; Kaercher, P.; Mao, Z.; Liu, J.; Wenk, H.R.; Prakapenka, V.B. Seismic anisotropy of the D″ layer induced by (001) deformation of post-perovskite. *Nat. Commun.* **2017**, *8*, 14669. [CrossRef] [PubMed]

69. Kubo, A.; Kiefer, B.; Shim, S.; Shen, G.; Prakapenka, V.B.; Duffy, T.S. Rietveld structure refinement of MgGeO₃ post-perovskite phase to 1 Mbar. *Am. Mineral.* **2008**, *93*, 965–976. [CrossRef]

70. Hustoft, J.; Shim, S.; Kubo, A.; Nishiyama, N. Raman spectroscopy of CaIrO₃ postperovskite up to 30 GPa. *Am. Mineral.* **2008**, *93*, 1654–1658. [CrossRef]

71. Tsuchiya, T.; Tsuchiya, J. Structure and elasticity of Cmcm CaIrO₃ and their pressure dependences: Ab initio calculations. *Phys. Rev. B* **2007**, *76*, 144119. [CrossRef]

72. Martin, C.D.; Crichton, W.A.; Liu, H.; Prakapenka, V.; Chen, J.; Parise, J.B. Phase transitions and compressibility of NaMgF₃ (Neighborite) in perovskite-and post-perovskite-related structures. *Geophys. Res. Lett.* **2006**, *33*, L11305. [CrossRef]

73. Dobson, D.P.; Hunt, S.A.; Lindsay-Scott, A.; Wood, I.G. Towards better analogues for MgSiO₃ post-perovskite: NaCoF₃ and NaNiF₃, two new recoverable fluoride post-perovskites. *Phys. Earth Planet. Inter.* **2011**, *189*, 171–175. [CrossRef]

74. Merkel, S.; Yagi, T. X-ray transparent gasket for diamond anvil cell high pressure experiments. *Rev. Sci. Instrum.* **2005**, *76*, 046109. [CrossRef]

75. Fei, Y.; Ricolleua, A.; Frank, M.; Mibe, K.; Shen, G.; Prakapenka, V. Toward an internally consistent pressure scale. *Proc. Natl. Acad. Sci. USA* **2007**, *104*, 9182–9186. [CrossRef]

76. Hammersley, A.P. *FIT2D: An Introduction and Overview*; ESRF97HA02T, ESRF Internal Report; ESRF: Grenoble, France, 1997; Volume 68, p. 58.

77. Lutterotti, L.; Matthies, S.; Wenk, H.; Schultz, A.S.; Richardson, J.W. Combined texture and structure analysis of deformed limestone from time-of-flight neutron diffraction spectra. *J. Appl. Phys.* **1997**, *81*, 594–600. [CrossRef]

78. Wenk, H.R.; Lutterotti, L.; Kaercher, P.; Kanitpanyacharoen, W.; Miyagi, L.; Vasin, R. Rietveld texture analysis from synchrotron diffraction images, I.I. Complex multiphase materials and diamond anvil cell experiments. *Powder Diffr.* **2014**, *29*, 220–232. [CrossRef]

79. Popa, N.C.; Balzar, D. An analytical approximation for a size-broadened profile given by the lognormal and gamma distributions. *J. Appl. Crystallogr.* **2002**, *35*, 338–346. [CrossRef]

80. Matthies, S.; Humbert, M. The Realization of the Concept of a Geometric Mean for Calculating Physical Constants of Polycrystalline Materials. *Phys. Status Solidi B* **1993**, *177*, K47–K50. [CrossRef]

81. Matthies, S.; Priesmeyer, H.G.; Daymond, M.R. On the diffractive determination of single-crystal elastic constants using polycrystalline samples. *J. Appl. Crystallogr.* **2001**, *34*, 585–601. [CrossRef]

82. Zhao, Y.; Weidner, D.J. The single crystal elastic moduli of neighborite. *Phys. Chem. Miner.* **1993**, *20*, 419–424. [CrossRef]

83. Hohenberg, P.; Kohn, W.J.P.R. Density functional theory (DFT). *Phys. Rev.* **1964**, *136*, B864. [CrossRef]

84. Kohn, W.; Sham, L.J. Self-consistent equations including exchange and correlation effects. *Phys. Rev.* **1965**, *140*, A1133. [CrossRef]

85. Blöchl, P.E. Projector augmented-wave method. *Phys. Rev. B* **1994**, *50*, 17953–17979. [CrossRef] [PubMed]

86. Kresse, G.; Joubert, D. From ultrasoft pseudopotentials to the projector augmented-wave method. *Phys. Rev. B* **1999**, *59*, 1758–1775. [CrossRef]

87. Kresse, G.; Furthmüller, J. Efficient iterative schemes for ab initio total-energy calculations using a plane-wave basis set. *Phys. Rev. B* **1996**, *54*, 11169–11186. [CrossRef]

88. Kresse, G.; Furthmüller, J. Efficiency of ab-initio total energy calculations for metals and semiconductors using a plane-wave basis set. *Comput. Mater. Sci.* **1996**, *6*, 15–50. [CrossRef]

89. Karki, B.B.; Stixrude, L.; Wentzcovitch, R.M. High-pressure elastic properties of major materials of Earth's mantle from first principles. *Rev. Geophys.* **2001**, *39*, 507–534. [CrossRef]

90. Perdew, J.P.; Burke, K.; Ernzerhof, M. Generalized gradient approximation made simple. *Phys. Rev. Lett.* **1996**, *77*, 3865–3868. [CrossRef]

91. Monkhorst, H.J.; Pack, J.D. Special points for Brillouin-zone integrations. *Phys. Rev. B* **1976**, *13*, 5188–5192. [CrossRef]

92. Jakymiw, C.; Vočadlo, L.; Dobson, D.P.; Bailey, E.; Thomson, A.R.; Brodholt, J.P.; Lindsay-Scott, A. The phase diagrams of $KCaF_3$ and $NaMgF_3$ by ab initio simulations. *Phys. Chem. Miner.* **2018**, *45*, 311–322. [CrossRef]

93. Arar, R.; Ouahrani, T.; Varshney, D.; Khenata, R.; Murtaza, G.; Rached, D.; Reshak, A.H. Structural, mechanical and electronic properties of sodium based fluoroperovskites NaXF3 (X = Mg, Zn) from first-principle calculations. *Mater. Sci. Semicond. Process.* **2015**, *33*, 127–135. [CrossRef]

94. Matthies, S.; Vinel, G.W. On the reproduction of the orientation distribution function of texturized samples from reduced pole figures using the conception of a conditional ghost correction. *Phys. Status Solidi (B)* **1982**, *112*, K111–K114. [CrossRef]

95. Speziale, S.; Shieh, S.R.; Duffy, T.S. High-pressure elasticity of calcium oxide: A comparison between Brillouin spectroscopy and radial X-ray diffraction. *J. Geophys. Res. Solid Earth* **2006**, *111*, B02203. [CrossRef]

96. Wenk, H.-R.; Matthies, S.; Donovan, J.; Chateigner, D. BEARTEX: A Windows-based program system for quantitative texture analysis. *J. Appl. Crystallogr.* **1998**, *31*, 262–269. [CrossRef]

97. Bunge, H. *Texture Analysis in Material Science: Mathematical Models*; Butterworths: London, UK, 1982.

98. Skemer, P.; Katayama, I.; Jiang, Z.; Karato, S.-I. The misorientation index: Development of a new method for calculating the strength of lattice-preferred orientation. *Tectonophysics* **2005**, *411*, 157–167. [CrossRef]

99. Bachmann, F.; Hielscher, R.; Schaeben, H. Texture analysis with MTEX–free and open source software toolbox. *Solid State Phenom.* **2010**, *160*, 63–68. [CrossRef]

100. Wang, H.; Wu, P.D.; Tomé, C.N.; Huang, Y. A finite strain elastic–viscoplastic self-consistent model for polycrystalline materials. *J. Mech. Phys. Solids* **2010**, *58*, 594–612. [CrossRef]

101. Dobson, D.P.; McCormack, R.; Hunt, S.A.; Ammann, M.W.; Weidner, D.; Li, L.; Wang, L. The relative strength of perovskite and post-perovskite $NaCoF_3$. *Mineral. Mag.* **2012**, *76*, 925–932. [CrossRef]

102. Kaercher, P.; Miyagi, L.; Kanitpanyacharoen, W.; Zepeda-Alarcon, E.; Wang, Y.; Parkinson, D.; Wenk, H.R. Two-phase deformation of lower mantle mineral analogs. *Earth Planet. Sci. Lett.* **2016**, *456*, 134–145. [CrossRef]

103. Merkel, S.; Wenk, H.-R.; Shu, J.; Shen, G.; Gillet, P.; Mao, H.K.; Hemley, R.J. Deformation of polycrystalline MgO at pressures of the lower mantle. *J. Geophys. Res. Solid Earth* **2002**, *107*, ECV-3. [CrossRef]

104. Wenk, H.-R.; Lonardelli, I.; Merkel, S.; Miyagi, L.; Pehl, J.; Speziale, S.; Tommaseo, C.E. Deformation textures produced in diamond anvil experiments, analysed in radial diffraction geometry. *J. Phys. Condens. Matter* **2006**, *18*, S933. [CrossRef] [PubMed]

105. Tsujino, N.; Nishihara, Y.; Yamazaki, D.; Seto, Y.; Higo, Y.; Takahashi, E. Mantle dynamics inferred from the crystallographic preferred orientation of bridgmanite. *Nature* **2016**, *539*, 81–84. [CrossRef] [PubMed]

106. Couper, S.; Speziale, S.; Marquardt, H.; Liermann, H.P.; Miyagi, L. Does heterogeneous strain act as a control on seismic anisotropy in Earth's lower mantle? *Front. Earth Sci.* **2020**, *8*, 540449. [CrossRef]

107. Cordier, P.; Ungár, T.; Zsoldos, L.; Tichy, G. Dislocation creep in $MgSiO_3$ perovskite at conditions of the Earth's uppermost lower mantle. *Nature* **2004**, *428*, 837–840. [CrossRef] [PubMed]

108. Wenk, H.-R.; Lonardeli, I.; Pehl, J.; Devine, J.; Prakapenka, V.; Shen, G.; Mao, H.K. In situ observation of texture development in olivine, ringwoodite, magnesiowüstite and silicate perovskite at high pressure. *Earth Planet. Sci. Lett.* **2004**, *226*, 507–519. [CrossRef]

109. Rokosky, J.M.; Lay, T.; Garnero, E.J. Small-scale lateral variations in azimuthally anisotropic D ″structure beneath the Cocos Plate. *Earth Planet. Sci. Lett.* **2006**, *248*, 411–425. [CrossRef]

110. Whittaker, S.; Thorne, M.S.; Schmerr, N.C.; Miyagi, L. Seismic array constraints on the D ″discontinuity beneath Central America. *J. Geophys. Res. Solid Earth* **2016**, *121*, 152–169. [CrossRef]

111. Walker, A.M.; Dobson, D.P.; Wookey, J.; Nowacki, A.; Forte, A.M. The anisotropic signal of topotaxy during phase transitions in D″. *Phys. Earth Planet. Inter.* **2018**, *276*, 159–171. [CrossRef]

112. Chandler, B.C.; Chen, L.W.; Li, M.; Romanowicz, B.; Wenk, H.R. Seismic anisotropy, dominant slip systems and phase transitions in the lowermost mantle. *Geophys. J. Int.* **2021**, *227*, 1665–1681. [CrossRef]

113. Kaercher, P.; Speziale, S.; Miyagi, L.; Kanitpanyacharoen, W.; Wenk, H.R. Crystallographic preferred orientation in wüstite (FeO) through the cubic-to-rhombohedral phase transition. *Phys. Chem. Miner.* **2012**, *39*, 613–626. [CrossRef]

114. Wookey, J.; Stackhouse, S.; Kendall, J.M.; Brodholt, J.; Price, G.D. Efficacy of the post-perovskite phase as an explanation for lowermost-mantle seismic properties. *Nature* **2005**, *438*, 1004–1007. [CrossRef]

115. Walker, A.M.; Forte, A.M.; Wookey, J.; Nowacki, A.; Kendall, J.M. Elastic anisotropy of D ″predicted from global models of mantle flow. *Geochem. Geophys. Geosyst.* **2011**, *12*, Q10006. [CrossRef]

116. Nowacki, A.; Walker, A.M.; Wookey, J.; Kendall, J.M. Evaluating post-perovskite as a cause of D″ anisotropy in regions of palaeosubduction. *Geophys. J. Int.* **2013**, *192*, 1085–1090. [CrossRef]

117. Jung, H.; Katayama, I.; Jiang, Z.; Hiraga, T.; Karato, S.I. Effect of water and stress on the lattice-preferred orientation of olivine. *Tectonophysics* **2006**, *421*, 1–22. [CrossRef]